Asynchronous space–time domain decomposition method with localized uncertainty quantification

Waad Subber[a], Karel Matouš[a,b,*]

[a] *Center for Shock Wave-processing of Advanced Reactive Materials (C-SWARM), University of Notre Dame, Notre Dame, IN 46556, United States*

[b] *Department of Aerospace and Mechanical Engineering, University of Notre Dame, Notre Dame, IN 46556, United States*

Highlights

- We develop an asynchronous space-time method for localized uncertainty assessment.
- We utilize polynomial chaos and domain decomposition with local Lagrange multipliers.
- We provide verification examples and convergence studies.
- We solve an impact problem with localized uncertainty in a region of interest.

Abstract

The computational cost associated with uncertainty quantification of engineering problems featuring localized phenomenon can be reduced by confining the random variability of the model parameters within a region of interest. In this case, a localized treatment of mesh and time resolutions is required to capture the effect of the confined material uncertainty on the global response. We present a computational approach for localized uncertainty quantification with the capability of asynchronous treatment of mesh and time resolutions. In particular, we allow each subdomain to have its local uncertainty representation and the corresponding mesh and time resolutions. As a result, computing resources can be directed toward a small region of interest where a model with high spatial and temporal resolutions is required. To verify the numerical implementation, we consider elastic wave propagation in an axially loaded beam. Moreover, we perform convergence studies with respect to the spatial and temporal discretizations as well as the size of an uncertain subdomain. A projectile impacting a composite sandwich plate is considered as an engineering application for the proposed method.

---

* Corresponding author at: Department of Aerospace and Mechanical Engineering, University of Notre Dame, Notre Dame, IN 46556, United States.

E-mail addresses: wsubber@nd.edu (W. Subber), kmatous@nd.edu (K. Matouš).

1. Introduction

Many practical engineering applications rely on the predictive capability of computer simulations [1]. Advances in computing power and numerical algorithms facilitate such predictions of large-scale applications using parallel computing (e.g., [2]). However, for the credibility of the computer predictions, it is critical to quantity uncertainty in the numerical simulations due to the random variability of the model parameters [3–6]. Uncertainty Quantification (UQ) using the traditional Monte-Carlo (MC) simulations can become computationally prohibitive when the computational cost of the underlying deterministic solver is already intensive [7,8]. These issues are especially apparent in problems with multiple spatial and temporal scales, where a large number of deterministic runs are required for convergence [1,9].

For a certain class of problems that are described by stochastic PDE's (i.e., PDE's with random coefficients), the Polynomial Chaos (PC) approach can provide a cost effective alternative for the uncertainty assessment of computationally intensive applications [5,7,10]. In the PC approach, the solution is represented by a functional expansion along the stochastic dimension and the coefficients of the expansion are determined either through Galerkin projection (intrusive) or pseudo-spectral projection (non-intrusive) [10,5,8]. Similar to MC sampling, the non-intrusive approach requires multiple calls to the underlying deterministic solver, which may become impractical for complex problems [8,11]. On the other hand, the intrusive approach generates a deterministic linear system to obtain the PC coefficients. However, as the size of the underlying deterministic problem and/or the dimension and order of the stochastic expansion grow, the linear system in the intrusive PC approach becomes exponentially larger in size and harder to solve [12,13]. Therefore, methodologies based on exploiting parallel algorithms are required to facilitate the intrusive PC implementation (i.e., to large-scale problems). Thus, customized PC solvers have been an active area of research. For example, multigrid methods [14,15], preconditioned iterative solvers [16–19], and domain decomposition techniques [20–24] have been utilized for the intrusive PC implementation. Another approach to reduce the computational cost of PC framework for UQ is stochastic model reduction (e.g., [25–28]).

Beside devising customized solvers for the intrusive PC implementations, domain decomposition methods have also been utilized for the localized treatment of uncertainty (e.g., [29–32]). The localization treatment requires a strategy to couple subdomains having different representation of uncertainty or subdomains with stochastic and deterministic models. Winter and Tartakovsky [29,30] introduced the random domain decomposition method to represent uncertainty in a partitioned domain as a two-scale random process. In their work, there is a global spatial scale of uncertainty in the extent of the subdomains and a local scale of uncertainty within each subdomains. Cottereau et al. [31] proposed a framework utilizing the Arlequin method to couple stochastic and deterministic subdomain models. In their framework, an overlap region between the subdomains is identified and a weighting function is introduced for the energy partitioning between the subdomain models. Hadigol et al. [32] adapted FETI algorithm and a *separated representation* for the stochastic expansion to formulate a framework which enables partitioned treatment of uncertainty.

In this work, we focus on reducing the computational cost of UQ in problems where a region of interest can be specified. In this region, the high resolution space and time discretization schemes are used for a stochastic model. Apart from the region of interest, low spatial and temporal resolutions are allowed for a stochastic model with low dimensional representation of the uncertainty (or a deterministic model). The framework can be viewed as a *reduced representation* of uncertainty for problems with localized features. The reduced representation is based on the localization treatment of the random material properties as well as the spatial and temporal resolutions. Therefore, computing power can be focused in a region of interest. To formulate the localized UQ framework, we extend the Parallel Asynchronous Space–Time Algorithm based on a Domain Decomposition Method (PASTA-DDM) [33] and incorporate intrusively the PC basis for the stochastic representation. Although we consider the intrusive approach for the PC implementation, we retain the same structure of the dual–primal linear system as in the deterministic PASTA-DDM [33]. The matrices in the stochastic dual–primal system have block sparsity structure compared to their counterparts in the deterministic case.

For the numerical illustration, we consider an axially loaded beam with the Young's modulus being a random field. We verify the numerical results of PASTA-DDM with Uncertainty Quantification (PASTA-DDM-UQ) using MC simulations. We quantify and provide convergence rates for the errors induced by coarsening the spatial and temporal resolutions, and coarsening and confining uncertainty. In the second example, we consider a *dog–bone* like specimen and study the dimension of the coupling mechanism, the sparsity structure of the arising linear system, and the effect of the localization region (location of the subdomain with random properties). Moreover, we consider a

projectile impacting a sandwich plate and show the potential of PASTA-DDM-UQ in reducing the computational cost of UQ in a complex simulation.

We organize the article as follows. Section 2 provides the mathematical formulation for PASTA-DDM-UQ. The spatial and time discretization schemes are presented in Section 3 and Section 4, respectively. Verification, convergence studies and application to an engineering problem are shown in Section 5. We draw conclusions in Section 6. In the Appendix, we present a Bayesian strategy to infer the localization region of interest.

2. Governing equations

Let $\Omega \subset \mathbb{R}^d$ be a spatial domain with boundary $\partial \Omega$ and let (Θ, Σ, P) be a probability space, where Θ is the sample space, Σ is the associated σ-algebra over Θ, and P represents an appropriate probability measure on Σ. Furthermore, let $\boldsymbol{\xi} = \{\xi_i(\theta)\}_{i=1}^M$, where $\theta \in \Theta$ represents a finite set of standard identically distributed random variables having a joint probability density function $p(\boldsymbol{\xi}) = p_1(\xi_1) \cdot p_2(\xi_2) \cdots p_M(\xi_M)$ with support $\Xi = \Xi_1 \times \Xi_2 \cdots \times \Xi_M \subset \mathbb{R}^M$. Then, we consider the following stochastic transient linear elasticity problem: Find a random function $\mathbf{u}(\mathbf{x}, t, \boldsymbol{\xi})$: $\Omega \times [0, T_f] \times \Xi \to \mathbb{R}$, such that the following equation holds

$$
\begin{aligned}
\rho \ddot{\mathbf{u}}(\mathbf{x}, t, \boldsymbol{\xi}) &= \nabla \cdot \boldsymbol{\sigma} + \mathbf{b} & \text{in } \Omega & \times [0, T_f] \times \Xi, \\
\mathbf{u}(\mathbf{x}, t, \boldsymbol{\xi}) &= \bar{\mathbf{u}} & \text{on } \partial \Omega_u & \times [0, T_f] \times \Xi, \\
\boldsymbol{\sigma} \cdot \mathbf{n} &= \bar{\mathbf{t}} & \text{on } \partial \Omega_t & \times [0, T_f] \times \Xi, \\
\mathbf{u}(\mathbf{x}, 0, \boldsymbol{\xi}) &= \mathbf{u}_0 & \text{in } \Omega & \times \Xi, \\
\dot{\mathbf{u}}(\mathbf{x}, 0, \boldsymbol{\xi}) &= \dot{\mathbf{u}}_0 & \text{in } \Omega & \times \Xi,
\end{aligned}
\tag{1}
$$

where ρ is the mass density, $\boldsymbol{\sigma}$ is the stress tensor, $\mathbf{u}$ is the displacement field, $\mathbf{b}$ is the body force, $\bar{\mathbf{u}}$ is the prescribed displacement on $\partial \Omega_u$, $\bar{\mathbf{t}}$ is the prescribed traction on $\partial \Omega_t$, $\mathbf{n}$ is a unit normal to the surface, and $\mathbf{u}_0$ and $\dot{\mathbf{u}}_0$ are the initial displacement and velocity, respectively.

For small deformations the infinitesimal strain tensor, $\boldsymbol{\varepsilon}$, is given by

$$
\boldsymbol{\varepsilon} = \frac{1}{2} \left(\nabla \mathbf{u} + \nabla \mathbf{u}^T \right).
\tag{2}
$$

Without loss of generality, we assume the elastic properties to be uncertain and define the following Kelvin-Voigt viscoelastic model [34] in which stress is proportional to both the strain $\boldsymbol{\varepsilon}$ and strain-rate $\dot{\boldsymbol{\varepsilon}}$ as

$$
\boldsymbol{\sigma} = \mathbf{D}(\boldsymbol{\xi}) : \boldsymbol{\varepsilon} + \widehat{\mathbf{D}} : \dot{\boldsymbol{\varepsilon}},
\tag{3}
$$

where $\mathbf{D}(\boldsymbol{\xi})$ is the linear elasticity tensor with uncertain parameters and $\widehat{\mathbf{D}}$ is a damping tensor assumed to be deterministic and based on the mean elasticity tensor as $\widehat{\mathbf{D}} = \eta \mathbf{D}^0$. Here, η is the damping coefficient and $\mathbf{D}^0$ is the mean elasticity tensor. We further assume that the Young's modulus can be represented by a random field, while the Poisson's ratio can be assumed deterministic. Note that the proposed algorithm is capable of handling arbitrary non-Gaussian representation yielding from considering both the Young's modulus and Poisson's ratio to be random. Representing the resulting non-Gaussian coefficients of the ratio of two random quantities in the constitutive matrix can be obtained by PC Galerkin projection [5,35,36]. However, in the subsequent examples, only Young's modulus is represented as a random field in order to avoid undue complexity in the numerical implementation.
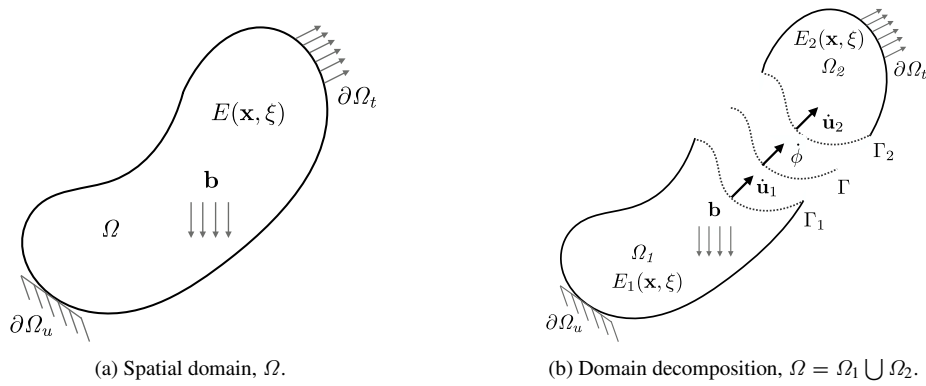
2.1. Representation of a random field

Given the mean field $E_0(\mathbf{x})$ and the covariance function $\mathbb{C}(\mathbf{x}_1, \mathbf{x}_2)$ of the Young's modulus, Karhunen–Loeve Expansion (KLE) is used to represent the random field as [5,7]

$$
E(\mathbf{x}, \boldsymbol{\xi}) = E_0(\mathbf{x}) + \tau \sum_{i=1}^M \sqrt{\kappa_i} \alpha_i(\mathbf{x}) \xi_i(\theta) = \sum_{i=0}^M E_i(\mathbf{x}) \xi_i(\theta),
\tag{4}
$$

where τ denotes the standard deviation of the field, κ_i, and $\alpha_i(\mathbf{x})$ are the eigenvalues and eigenfunctions of the covariance function, respectively. Here, we denote the KLE coefficients $E_i(\mathbf{x}) = \tau \sqrt{\kappa_i} \alpha_i(\mathbf{x})$, for $i > 0$, and set $\xi_0(\theta) = 1$. The eigenpairs $\{\kappa_i, \alpha_i(\mathbf{x})\}$ can be obtained from the solution of the following integral eigenvalue problem [5,7]

$$
\int_\Omega \mathbb{C}(\mathbf{x}_1, \mathbf{x}_2) \alpha_i(\mathbf{x}_1) d\mathbf{x}_1 = \kappa_i \alpha_i(\mathbf{x}_2).
\tag{5}
$$

(a) Spatial domain, Ω.   (b) Domain decomposition, $\Omega = \Omega_1 \bigcup \Omega_2$.

Fig. 1. An arbitrary computational domain Ω with a random material property (i.e., $E(\mathbf{x}, \boldsymbol{\xi})$) and its partitioning into two non-overlapping subdomains Ω_1 and Ω_2. The local interfaces of Ω_1 and Ω_2 are denoted by Γ_1 and Γ_2, respectively. The global interface is denoted by Γ. The velocities on the boundaries Γ_1, Γ_2, and Γ are denoted by $\dot{\mathbf{u}}_1$, $\dot{\mathbf{u}}_2$, and $\dot{\boldsymbol{\phi}}$, respectively.

Consequently, the random elasticity tensor $\mathbf{D}(\boldsymbol{\xi})$ is represented as

$$\mathbf{D}(\boldsymbol{\xi}) = \sum_{i=0}^{M} \mathbf{D}^i \xi_i(\theta), \tag{6}$$

where $\mathbf{D}^i$ are the KLE coefficients of the elasticity tensor associated with the KLE coefficients of the Young's modulus $E_i(\mathbf{x})$ in Eq. (4).

2.2. PASTA-DDM with uncertainty quantification (PASTA-DDM-UQ)

For large-scale problems with localized uncertainty, a domain decomposition based algorithm such as PASTA-DDM [33] becomes a natural choice. In this section, we summarize our PASTA-DDM method and extend it to problems with uncertainty. In PASTA-DDM framework, the physical domain Ω, Fig. 1, is partitioned into n_s non-overlapping subdomains $\Omega_s, 1 \leqslant s \leqslant n_s$ such that:

$$\Omega = \bigcup_{s=1}^{n_s} \Omega_s, \quad \Omega_s \bigcap \Omega_r = \emptyset \text{ for } s \neq r, \quad \Gamma = \bigcup_{s=1}^{n_s} \Gamma_s, \quad \Gamma_s = \partial \Omega_s \setminus \partial \Omega. \tag{7}$$

This decomposition is supplemented with transmission conditions to satisfy the continuity requirement of the solution field.

Consequently, Eq. (1) can be transformed into the following constrained minimization problem: Find a random function $\mathbf{u}(\mathbf{x}, t, \boldsymbol{\xi}) : \Omega \times [0, T_f] \times \Xi \to \mathbb{R}$, such that

$$\mathcal{L}(\mathbf{u}_s, \dot{\mathbf{u}}_s) = \sum_{s=1}^{n_s} (\mathcal{T}(\dot{\mathbf{u}}_s) - \mathcal{V}(\mathbf{u}_s)) \to \min, \tag{8}$$

$$\mathcal{Q}(\dot{\mathbf{u}}_s) = \sum_{s=1}^{n_s} \frac{1}{2} \int_{\Xi} \int_{\Omega_s} \dot{\boldsymbol{\varepsilon}}_s : \widehat{\mathbf{D}}_s : \dot{\boldsymbol{\varepsilon}}_s \, d\Omega d\Xi, \tag{9}$$

$$\text{subject to: } \int_{\Xi} \int_{\Gamma} (\dot{\mathbf{u}}_s - \dot{\boldsymbol{\phi}}) \, d\Gamma d\Xi = \mathbf{0}, \quad s = 1, \ldots, n_s, \tag{10}$$

where $\mathcal{L}(\mathbf{u}_s, \dot{\mathbf{u}}_s)$ is the Lagrangian of the system, $\mathcal{T}(\dot{\mathbf{u}}_s)$ denotes the subdomain kinetic energy, $\mathcal{V}(\mathbf{u}_s)$ is the subdomain potential energy, and $\mathcal{Q}(\dot{\mathbf{u}}_s)$ is the dissipation function. Here, $\dot{\mathbf{u}}_s$ represents the local subdomain velocity and $\dot{\boldsymbol{\phi}}$ is the velocity of the common interface (frame) (see Fig. 1(b)). We denote the expectation operator as $\int_{\Xi}(\bullet)p(\boldsymbol{\xi})d\boldsymbol{\xi} = \int_{\Xi}(\bullet)d\Xi$.

Utilizing the local Lagrange multipliers $\boldsymbol{\lambda}_s$ to enforce the common interface kinematic constraint given by Eq. (10), the augmented Lagrangian yields

$$\tilde{\mathcal{L}}(\mathbf{u}_s, \dot{\mathbf{u}}_s, \boldsymbol{\lambda}_s, \dot{\boldsymbol{\phi}}) = \sum_{s=1}^{n_s} \int_{\Xi} \left(\frac{1}{2} \int_{\Omega_s} \rho_s \dot{\mathbf{u}}_s \cdot \dot{\mathbf{u}}_s \, \mathrm{d}\Omega - \frac{1}{2} \int_{\Omega_s} \boldsymbol{\varepsilon}_s : \boldsymbol{\sigma}_s \, \mathrm{d}\Omega \right.$$
$$\left. + \int_{\Omega_s} \mathbf{u}_s \cdot \mathbf{b}_s \, \mathrm{d}\Omega + \int_{\partial \Omega_t} \mathbf{u}_s \cdot \bar{\mathbf{t}}_s \, \mathrm{d}\Gamma + \int_{\Gamma} \boldsymbol{\lambda}_s \cdot (\dot{\mathbf{u}}_s - \dot{\boldsymbol{\phi}}) \, \mathrm{d}\Gamma \right) \mathrm{d}\Xi. \tag{11}$$

The Hamilton's principle with the dissipation term reads [37]

$$\int_0^{T_f} \left(\delta \tilde{\mathcal{L}} - \frac{\partial \mathcal{Q}}{\partial \dot{\boldsymbol{\varepsilon}}_s} : \delta \boldsymbol{\varepsilon}_s \right) \mathrm{dt} = 0, \tag{12}$$

where $\delta \tilde{\mathcal{L}}$ is the first variation of the augmented Lagrangian:

$$\delta \tilde{\mathcal{L}} = \sum_{s=1}^{n_s} \int_{\Xi} \left[\int_{\Omega_s} \rho_s \delta \dot{\mathbf{u}}_s \cdot \dot{\mathbf{u}}_s \, \mathrm{d}\Omega - \int_{\Omega_s} \delta \boldsymbol{\varepsilon}_s : \mathbf{D}_s(\boldsymbol{\xi}) : \boldsymbol{\varepsilon}_s \, \mathrm{d}\Omega + \right.$$
$$\int_{\Omega_s} \delta \mathbf{u}_s \cdot \mathbf{b}_s \, \mathrm{d}\Omega + \int_{\partial \Omega_t} \delta \mathbf{u}_s \cdot \bar{\mathbf{t}}_s \, \mathrm{d}\Gamma + \int_{\Gamma} \delta \boldsymbol{\lambda}_s \cdot (\dot{\mathbf{u}}_s - \dot{\boldsymbol{\phi}}) \, \mathrm{d}\Gamma +$$
$$\left. \int_{\Gamma} \delta \dot{\mathbf{u}}_s \cdot \boldsymbol{\lambda}_s \mathrm{d}\Gamma - \int_{\Gamma} \delta \dot{\boldsymbol{\phi}} \cdot \boldsymbol{\lambda}_s \, \mathrm{d}\Gamma \right] \mathrm{d}\Xi. \tag{13}$$

Utilizing Eqs. (9) and (13), the Hamilton's principle in Eq. (12) leads to the following three equations for a typical subdomain Ω_s. The stochastic constrained equation of motion:

$$\int_{\Xi} \int_{\Omega_s} \rho_s \ddot{\mathbf{u}}_s \cdot \delta \mathbf{u}_s \, \mathrm{d}\Omega \, \mathrm{d}\Xi + \int_{\Xi} \int_{\Omega_s} \dot{\boldsymbol{\varepsilon}}_s : \widehat{\mathbf{D}}_s : \delta \boldsymbol{\varepsilon}_s \, \mathrm{d}\Omega \, \mathrm{d}\Xi \tag{14}$$
$$+ \int_{\Xi} \int_{\Omega_s} \boldsymbol{\varepsilon}_s : \mathbf{D}_s(\boldsymbol{\xi}) : \delta \boldsymbol{\varepsilon}_s \, \mathrm{d}\Omega \, \mathrm{d}\Xi + \int_{\Xi} \int_{\Gamma_s} \dot{\boldsymbol{\lambda}}_s \cdot \delta \mathbf{u}_s \, \mathrm{d}\Gamma \, \mathrm{d}\Xi$$
$$= \int_{\Xi} \int_{\Omega_s} \delta \mathbf{u}_s \cdot \mathbf{b}_s \, \mathrm{d}\Omega \, \mathrm{d}\Xi \boldsymbol{\lambda}_s + \int_{\Xi} \int_{\partial \Omega_t} \delta \mathbf{u}_s \cdot \bar{\mathbf{t}}_s \, \mathrm{d}\Gamma \, \mathrm{d}\Xi.$$

The stochastic kinematic constraint coupling the subdomains:

$$\int_{\Xi} \int_{\Gamma} \delta \boldsymbol{\lambda}_s \cdot (\dot{\mathbf{u}}_s - \dot{\boldsymbol{\phi}}) \, \mathrm{d}\Gamma \, \mathrm{d}\Xi = \mathbf{0}. \tag{15}$$

The stochastic equilibrium equation among the subdomains:

$$- \sum_{s=1}^{n_s} \int_{\Xi} \int_{\Gamma} \delta \boldsymbol{\phi} \cdot \dot{\boldsymbol{\lambda}}_s \, \mathrm{d}\Gamma \, \mathrm{d}\Xi = \mathbf{0}. \tag{16}$$

Next, we seek an approximate solution to the weak problem in a finite dimensional tensor product space of the spatial finite element and stochastic multivariate polynomial. This tensor space $\mathcal{H}(\Omega_s \times \Xi)$ can be expressed as $\mathcal{H} = \mathcal{H}(\Omega_s) \otimes L_2(\Xi)$, where $\mathcal{H}(\Omega_s)$ is the traditional Hilbert space and $L_2(\Xi)$ is the space of second order random variables [38].

The solution to the stochastic weak problem, Eqs. (14)–(16), can be obtained either using the intrusive or non-intrusive approach. The selection of intrusive versus non-intrusive implementation is problem dependent and requires careful considerations. In the intrusive approach, an optimal accuracy of the solution can be obtained since the error resulting from the finite PC representation is orthogonal to the stochastic space spanned by the PC basis [8,39]. On the other hand in the non-intrusive approach, the error due to the integration rule can cause aliasing [8]. Furthermore, for problems when a single deterministic run (required by the non-intrusive approach) is computationally intensive, the intrusive approach can provide a faster execution time given the development of efficient solvers [8,39]. Since the main objective of this work is to develop a framework for reducing the computational cost of UQ in problems with a localized region of interest, we follow the intrusive approach.

3. The stochastic finite element discretization

Let the spatial subdomain Ω_s be triangulated with finite elements of size h^s and let the associated finite element subspaces $\mathcal{X}_h^s \subset H_0^1(\Omega_s)$, $\mathcal{Y}_h^s \subset H_0^1(\Omega_s)$, and $\mathcal{Z}_h^s \subset H_0^1(\Omega_s)$ for the displacement, Lagrange multipliers, and the common interface variable be spanned by nodal bases functions $\{\mathbf{N}_u^i(\mathbf{x})\}_{i=1}^L$, $\{\mathbf{N}_\lambda^i(\mathbf{x})\}_{i=1}^L$, and $\{\mathbf{N}_\phi^i(\mathbf{x})\}_{i=1}^L$, respectively. Furthermore, for the stochastic discretization, let $\mathcal{W}_p \subset L_2(\Xi)$ be a finite dimensional space of square-integrable random variables spanned by the polynomial chaos basis functions $\{\Psi^j(\boldsymbol{\xi})\}_{j=0}^N$ of the random variables $\boldsymbol{\xi}(\theta) = \{\xi_i(\theta)\}_{i=1}^M$. Thus, the approximated stochastic finite element solution in the discrete tensor product space $\mathcal{X}_h^s \otimes \mathcal{W}_p \subset H_0^1(\Omega_s) \otimes L_2(\Xi)$, $\mathcal{Y}_h^s \otimes \mathcal{W}_p \subset H_0^1(\Omega_s) \otimes L_2(\Xi)$, and $\mathcal{Z}_h^s \otimes \mathcal{W}_p \subset H_0^1(\Omega_s) \otimes L_2(\Xi)$ can be expressed as

$$
\begin{aligned}
\mathbf{u}_s^{hp}(\mathbf{x}, \boldsymbol{\xi}, t) &= \sum_{j=0}^N \sum_{i=1}^L \mathbf{N}_u^i(\mathbf{x}) \, \Psi^j(\boldsymbol{\xi}) \tilde{\mathbf{u}}_s^{ij}(t), \\
\boldsymbol{\lambda}_s^{hp}(\mathbf{x}, \boldsymbol{\xi}, t) &= \sum_{j=0}^N \sum_{i=1}^L \mathbf{N}_\lambda^i(\mathbf{x}) \, \Psi^j(\boldsymbol{\xi}) \tilde{\boldsymbol{\lambda}}_s^{ij}(t), \\
\boldsymbol{\phi}_s^{hp}(\mathbf{x}, \boldsymbol{\xi}, t) &= \sum_{j=0}^N \sum_{i=1}^L \mathbf{N}_\phi^i(\mathbf{x}) \, \Psi^j(\boldsymbol{\xi}) \tilde{\boldsymbol{\phi}}_s^{ij}(t).
\end{aligned}
\tag{17}
$$

Substituting these discrete fields in the weak form Eqs. (14)–(16) gives the following semi-discretized stochastic equation of motion, the kinematic constraint, and the equilibrium equation at the interface

$$
\mathbf{M}_s \ddot{\mathbf{U}}_s(t) \mathbf{Q}^0 + \mathbf{C}_s \dot{\mathbf{U}}_s(t) \mathbf{Q}^0 + \sum_{i=0}^M \mathbf{K}_s^i \mathbf{U}_s(t) \mathbf{Q}^i + \mathbf{E}_s^T \boldsymbol{\Lambda}_s(t) \mathbf{Q}^0 = \mathbf{F}_s(t),
\tag{18}
$$

$$
\mathbf{E}_s \dot{\mathbf{U}}_s(t) \mathbf{Q}^0 - \mathbf{B}_s \boldsymbol{\Phi}(t) \mathbf{Q}^0 = \mathbf{0},
\tag{19}
$$

$$
-\sum_{s=1}^{n_s} \mathbf{B}_s^T \boldsymbol{\Lambda}_s(t) \mathbf{Q}^0 = \mathbf{0}.
\tag{20}
$$

We drop the nodal finite element marks (tilde) for brevity of the representation and define the following matrices:

$$
\begin{aligned}
\mathbf{Q}^0 &= \int_\Xi \boldsymbol{\Psi} \boldsymbol{\Psi} \mathrm{d}\Xi, \quad \mathbf{Q}^i = \int_\Xi \boldsymbol{\Psi} \boldsymbol{\xi}^i \boldsymbol{\Psi} \mathrm{d}\Xi, \quad \mathbf{M}_s = \int_{\Omega_s} \rho_s \mathbf{N}_u^T \mathbf{N}_u \mathrm{d}\Omega, \\
\mathbf{C}_s &= \int_{\Omega_s} \mathbf{H}_u^T \widehat{\mathbf{D}}_s \mathbf{H}_u \mathrm{d}\Omega, \quad \mathbf{K}_s^i = \int_{\Omega_s} \mathbf{H}_u^T \mathbf{D}_s^i \mathbf{H}_u \mathrm{d}\Omega, \quad \mathbf{E}_s = \int_{\Omega_s} \mathbf{N}_\lambda^T \mathbf{N}_u \mathrm{d}\Gamma, \\
\mathbf{B}_s &= \int_{\Omega_s} \mathbf{N}_\lambda^T \mathbf{N}_\phi \mathrm{d}\Gamma, \quad \mathbf{U}_s(t) = \{\mathbf{u}_s^0(t), \dots, \mathbf{u}_s^N(t)\}, \\
\boldsymbol{\Lambda}_s(t) &= \{\dot{\boldsymbol{\lambda}}_s^0(t), \dots, \dot{\boldsymbol{\lambda}}_s^N(t)\}, \quad \boldsymbol{\Phi}(t) = \{\dot{\boldsymbol{\phi}}^0(t), \dots, \dot{\boldsymbol{\phi}}^N(t)\}.
\end{aligned}
$$

Here, $\mathbf{H}_u$ is the displacement–strain matrix.

At this stage, it is worth mentioning that in the case of non-matching meshes along the interfaces, the discrete subdomain trace operators ($\mathbf{E}_s$ and $\mathbf{B}_s$) in Eq. (19) are not node-to-node restriction matrices. Therefore the finite element discretization, Eqs. (18)–(20), must satisfy the Ladyzhenskaya–Babuška–Brezzi (*inf–sup*) stability condition [40]. In the original PASTA-DDM work [33], we have shown that our three-field method satisfies the *inf–sup* condition for the deterministic case. For the stochastic case, since we use a discrete tensor product space, the *inf–sup* condition holds, provided that the material parameters are bounded.

4. Time discretization

In this section, we briefly summarize the asynchronous time integration method presented in Subber and Matouš [33]. Let the integration time $[T_0, T_f]$ be divided into n_f time steps and let n_{t_s} denote the number of the subdomain time steps. Then, the global synchronization ΔT and the local subdomain Δt_s time steps are defined as

$$
\Delta T = \frac{T_f - T_0}{n_f} \quad \text{and} \quad \Delta t_s = \frac{\Delta T}{n_{t_s}}.
\tag{21}
$$

The Newmark time integration scheme, with local integration parameters γ_s and β_s, is used to advance the stochastic system one time step as

$$\dot{\mathbf{U}}_s^{k+1} = \dot{\mathbf{U}}_s^k + (1 - \gamma_s)\Delta t_s \ddot{\mathbf{U}}_s^k + \gamma_s \Delta t_s \ddot{\mathbf{U}}_s^{k+1}, \tag{22}$$

$$\mathbf{U}_s^{k+1} = \mathbf{U}_s^k + \Delta t_s \dot{\mathbf{U}}_s^k + \left(\frac{1}{2} - \beta_s\right)\Delta t_s^2 \ddot{\mathbf{U}}_s^k + \beta \Delta t_s^2 \ddot{\mathbf{U}}_s^{k+1}. \tag{23}$$

Furthermore, a generalized α method is used for the Lagrange multipliers as

$$\boldsymbol{\Lambda}_s^k = S^k \boldsymbol{\Lambda}_s^n + T^k \boldsymbol{\Lambda}_s^{n+1}, \tag{24}$$

where the linear functions read $S^k = 1 - k/n_{t_s}$ and $T^k = k/n_{t_s}$. Accordingly, the full discrete system (after vectorization) yields

$$\mathcal{M}_s \ddot{\mathcal{U}}_s^{k+1} + \mathcal{C}_s \dot{\mathcal{U}}_s^{k+1} + \mathcal{K}_s \mathcal{U}_s^{k+1} + T^{k+1}\mathcal{E}_s^T \mathcal{L}_s^{n+1} = \mathcal{F}_s^{k+1} - S^{k+1}\mathcal{E}_s^T \mathcal{L}_s^n, \tag{25}$$

$$-\gamma_s \Delta t_s \ddot{\mathcal{U}}_s^{k+1} + \dot{\mathcal{U}}_s^{k+1} = -(1 - \gamma_s)\Delta t_s \ddot{\mathcal{U}}_s^k - \dot{\mathcal{U}}_s^k, \tag{26}$$

$$-\beta_s \Delta t_s^2 \ddot{\mathcal{U}}_s^{k+1} + \mathcal{U}_s^{k+1} = -\left(\frac{1}{2} - \beta_s\right)\Delta t_s^2 \ddot{\mathcal{U}}_s^k - \Delta t_s \dot{\mathcal{U}}_s^k - \mathcal{U}_s^k,$$

$$\mathcal{E}_s \dot{\mathcal{U}}_s^{k+1} - \mathcal{E}_s \mathcal{P}_s^{k+1} = \mathbf{0}, \quad \text{if} \quad k \neq n_{t_s} - 1,$$

$$\mathcal{E}_s \dot{\mathcal{U}}_s^{k+1} - \mathcal{B}_s \mathcal{P}^{n+1} = \mathbf{0}, \quad \text{if} \quad k = n_{t_s} - 1, \tag{29}$$

$$\sum_{s=1}^{n_s} -\mathcal{B}_s^T \mathcal{L}_s^{n+1} = \mathbf{0}, \tag{30}$$

where vectorization, vec($\bullet$), is employed which concatenates the columns of a matrix into one column vector. Furthermore, we define the following vectors and matrices

$$\mathcal{M}_s = \mathbf{Q}^0 \otimes \mathbf{M}_s, \quad \mathcal{C}_s = \mathbf{Q}^0 \otimes \mathbf{C}_s, \quad \mathcal{K}_s = \sum_{i=0}^M \mathbf{Q}^i \otimes \mathbf{K}_s^i,$$

$$\mathcal{E}_s = \mathbf{Q}^0 \otimes \mathbf{E}_s, \quad \mathcal{B}_s = \mathbf{Q}^0 \otimes \mathbf{B}_s, \quad \mathcal{L}_s = \text{vec}(\boldsymbol{\Lambda}_s),$$

$$\mathcal{U}_s = \text{vec}(\mathbf{U}_s), \quad \mathcal{F}_s = \text{vec}(\mathbf{F}_s), \quad \mathcal{P} = \text{vec}(\boldsymbol{\Phi}).$$

Note that the structure of the full dual–primal system for PASTA-DDM-UQ in the stochastic setting is the same as that of the original deterministic PASTA-DDM [33]. The only difference is the block sparsity structure of the matrices. We will comment on the matrix structure in Section 5.2.

5. Numerical examples

In this section, we present the numerical results of our framework for asynchronous space–time algorithm with uncertainty quantification. First, we verify our computer implementation of PASTA-DDM-UQ with the traditional Monte-Carlo (MC) simulations. We study different approaches for reducing the computational cost of uncertainty quantification. We assess and provide convergence rates for the error that is associated with coarsening the space and time discretizations, and confining uncertainty. Furthermore, we study the dimension of the coupling mechanism, sparsity pattern and the localization region. Then, we show the capability of PASTA-DDM-UQ to solve engineering problems by considering a composite plate impacted by a projectile. We investigate and study the effect of combining asynchronous space and time refinements with localized uncertainty.

5.1. Verification and convergence studies

For the numerical verification, we consider an axially loaded beam (3.0 × 0.5 m) clamped at the right-hand side while a time-dependent traction vector is applied on the left-hand side as shown in Fig. 2. For PASTA-DDM-UQ implementation, the computational domain is decomposed into three subdomains $\Omega = \cup_{s=1}^3 \Omega_s$. The horizontal traction is defined as $F(t) = F_0 \cos(\omega t)$, where $F_0 = 2100\,\text{kN/m}$ and $\omega = 1.8\,\text{s}^{-1}$. The quantities of interest (QOIs) are the horizontal component of the displacement and velocity at point P located in the middle of the domain as marked in Fig. 2.
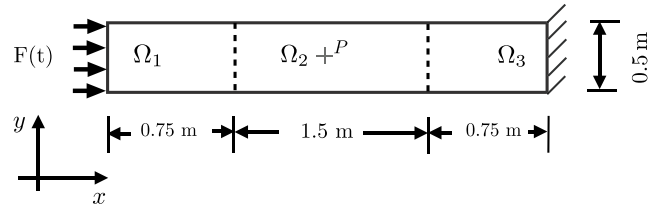
Fig. 2. Axially loaded beam exited by a time-dependent traction vector. The QOIs are the displacement and velocity at point P located at $(1.5, 0.25)$ m.

For the numerical implementation, the Young's modulus ($E(\mathbf{x}, \boldsymbol{\xi})$, $\mathbf{x} \in \Omega$, $\Omega = \cup_{s=1}^{3} \Omega_s$) is represented by a random field having a constant mean $E_0 = 81.9$ kPa and the following exponential covariance function

$$\mathbb{C}(\mathbf{x}_1, \mathbf{x}_2) = \tau^2 \exp\left(-\frac{|x_1 - x_2|}{b_x} - \frac{|y_1 - y_2|}{b_y}\right), \tag{31}$$

where the standard deviation is $\tau = 12.285$ kPa, and the correlation lengths are $b_x = 6.0$ m and $b_y = 3.0$ m. The analytical expressions for the eigenvalues and the associated eigenfunctions for this covariance function are available in many textbooks on UQ (e.g., [5–8]). Typically for computer implementation, the KLE is truncated such that a given amount of the random field variance is retained [5–8]. In other words, the sum of the neglected eigenvalues (the mean-square-error) is sufficiently small compared to the sum of the first M terms [5–8]. In the numerical examples, we truncate KLE such that 90% of the total variance is captured by the first M terms. Although not exercised in this work, a scaling of the eigenvalues can be considered such that the total variance is conserved. This approach may enhance the accuracy of the KLE representation of the input random field, but not the localized UQ framework.

The Young's modules field is approximated by KLE with two random variables. Poisson's ratio and mass density are assumed to be deterministic quantities and their assigned values are $\nu = 0.3$ and $\rho = 7800$ kg/m³. The damping matrix is also deterministic and based on the mean property of the elasticity matrix with a damping coefficient $\eta = 15\%$.

### 5.1.1. Verification of uncertainty representation

To verify the computer implementation of PASTA-DD-UQ, MC method without domain decomposition is considered. For the sampling procedure, Latin Hypercube Sampling (LHS) technique is used with 1000 samples. The computational domain is discretized using mesh density $h = 0.03125$ m leading to 3072 elements and 1649 nodes. Traditional piecewise linear finite elements are used for the displacement, the common interface variable, and the Lagrange multipliers [33]. Three subdomains with matching discretization along the interfaces are used in this example. The system is integrated with uniform time step $\Delta t = 0.025$ s up to the final time $T_f = 50$ s. We use intrusive implementation of PC and employ the second ($PC2$), fourth ($PC4$), and sixth order ($PC6$) expansions.

Fig. 3 shows the mean and the standard deviation (Std) of the horizontal component of the displacement at point P, while Fig. 4 displays the phase space diagrams. It can be seen that the fourth order PC representation is in good agreement with MC results. Increasing the PC order from fourth (15 terms in the expansion) to sixth (28 terms in the expansion) qualitatively does not change the accuracy of the solution. Note that the presence of random Young's modulus leads to a discrepancy of 16% in the maximum amplitude of the displacement and velocity means compared to the deterministic solution. Thus, this example provides a reasonable testbed.

To assess the quality of the PASTA-DDM-UQ solution, we define the following error measures for both the displacement and velocity at point P:

$$\begin{aligned}
\mathcal{E}_{PC}(\text{MSTD}(\mathbb{X})) &= \frac{\overline{\text{MSTD}}_{PC6}(\mathbb{X}) - \text{MSTD}(\mathbb{X})}{\max\left(\overline{\text{MSTD}}_{PC6}(\mathbb{X})\right)} \times 100 \, [\%], \\
\mathcal{E}_{MC}(\text{MSTD}(\mathbb{X})) &= \frac{\overline{\text{MSTD}}_{MC}(\mathbb{X}) - \text{MSTD}(\mathbb{X})}{\max\left(\overline{\text{MSTD}}_{MC}(\mathbb{X})\right)} \times 100 \, [\%].
\end{aligned} \tag{32}$$

Here, $\mathcal{E}_{PC}(\bullet)$ denotes the error with respect to sixth order PC representation and $\mathcal{E}_{MC(\bullet)}$ indicates the error with respect to MC simulations. The quantity MSTD represents either the mean or the standard deviation and the dummy variable

(a) Mean.

(b) Standard deviation.
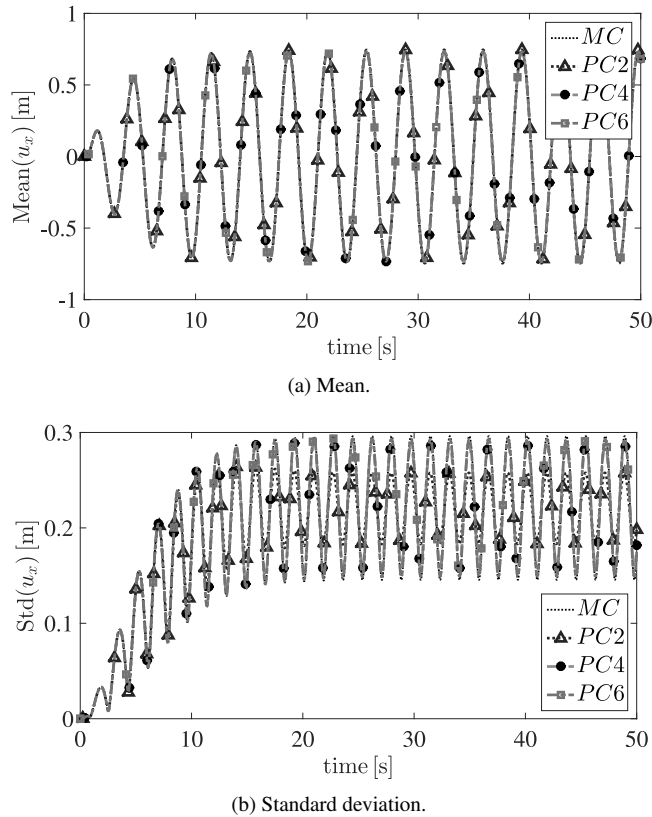
Fig. 3. The mean (a) and the standard deviation (b) of the horizontal component of the displacement at point P. MC indicates Monte-Carlo simulations, $PC2$, $PC4$, and $PC6$ are the second, fourth, and sixth order PC expansion, respectively.

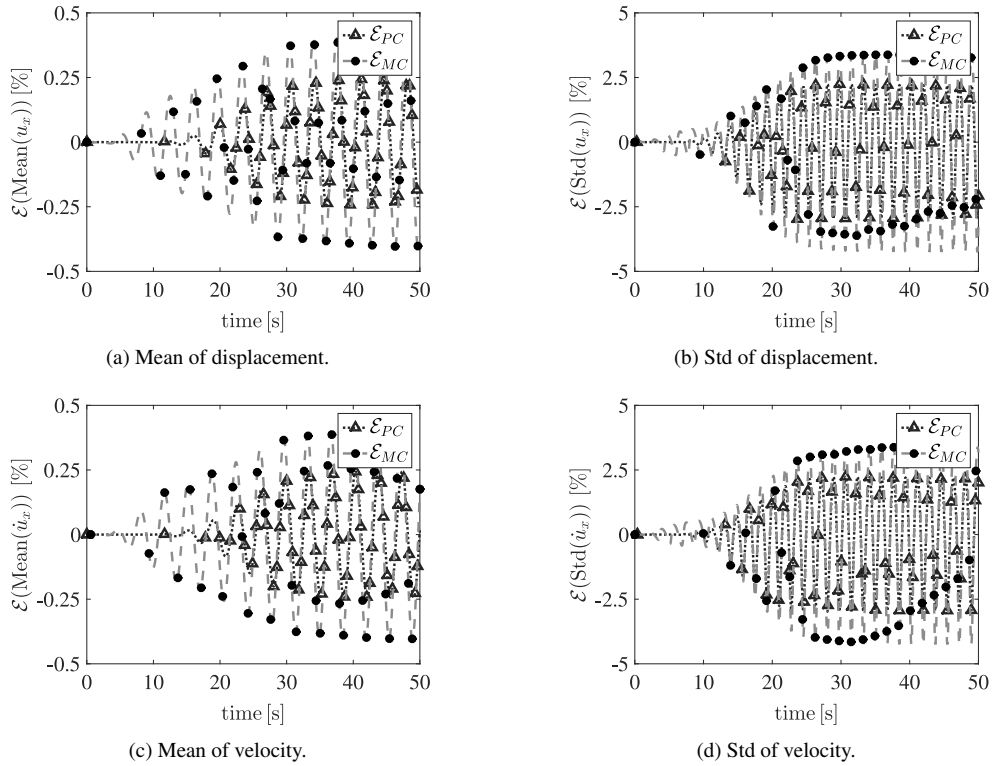$\mathbb{X}$ is either the horizontal displacement u_x or velocity $\dot{u}_x$ at point P. The quantity $\overline{\text{MSTD}}$ stands for the reference solution.

In Fig. 5, we show the relative percentage error of the mean and Std of the displacement and velocity at point P using fourth order PC expansion. The relative percentage error in the displacement and the velocity have the same trend. The maximum value of the error in the mean for both the displacement and velocity is less than 0.5%. Moreover, the error in the Std is less than 5% for both the displacement and velocity. The larger error in the Std compared to the mean can be attributed to the fact that the higher order of the chaos expansion is required to accurately obtain the higher order moments in PC expansion [41,42]. Based on these percentage error values, in the following subsections we consider the fourth order PC expansion as an accurate representation of uncertainty in the response.

We note that this PC order is kept constant in all subdomains. To vary the PC order across the interface, a coupling mechanism for the non-conforming PC coefficients would be required. This would be analogous to the case of non-conforming meshes, but it is out of the scope of this work.

5.1.2. Effect of mesh incompatibility

For uncertainty quantification, when the solution varies slowly, a fine mesh resolution might not be needed everywhere in the domain. In what follows, we investigate the effect of coarsening the mesh apart from the region of interest on the accuracy of the solution. In particular, we consider three non-matching mesh discretizations listed in Table 1. The meshes are defined such that a fine mesh resolution is kept in Ω_2, where the QOIs are located, and a coarser resolution is allowed in Ω_1 and Ω_3. In Fig. 6, we show mesh (b) which consists of 1632 elements and 903 nodes. This mesh has about 50% less elements than the full compatible mesh with $h = 0.03125$ m used in the previous Section 5.1.1.

(a) Mean.

(b) Standard deviation.
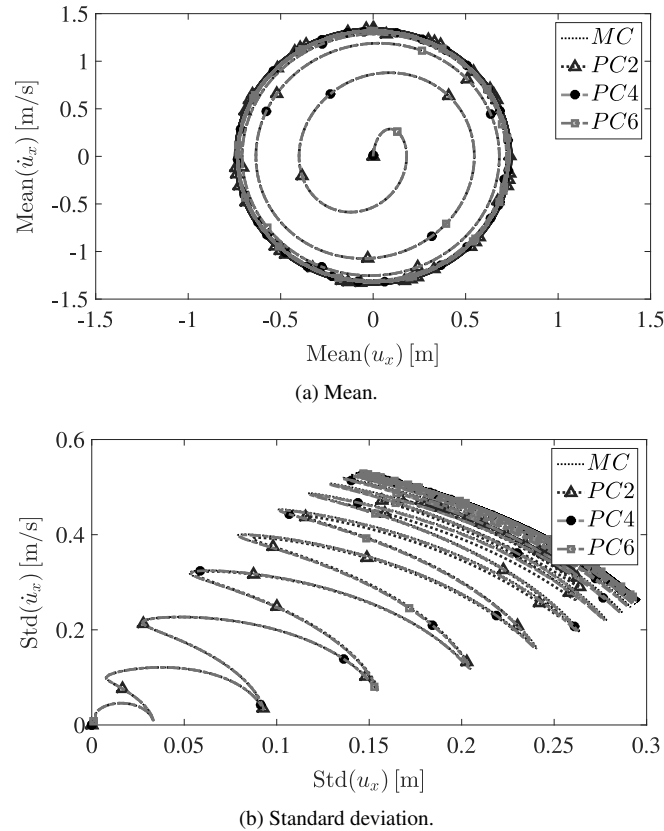
Fig. 4. The phase space diagram for (a) the mean and (b) the standard deviation at point P. MC indicates Monte-Carlo simulations, $PC2$, $PC4$, and $PC6$ are the second, fourth, and sixth order PC expansion, respectively.

Table 1
Incompatible mesh discretizations.

Mesh	h_1 [m]	h_2 [m]	h_3 [m]	h_1:h_2:h_3
(a)	0.0625	0.03125	0.0625	1:2:1
(b)	0.1250	0.03125	0.1250	1:4:1
(c)	0.2500	0.03125	0.2500	1:8:1

For Mesh (b) with uniform time increment $\Delta t_s = 0.025$ s and fourth order PC expansion, the relative percentage error of the mean and standard deviation of the displacement and velocity at point P are shown in Fig. 7. We use the error measures defined in Eq. (32). Both the errors in the displacement and velocity have the same trend. A reduction of about 50% in the number of elements leads to less than 1.5% maximum error in the mean displacement and velocity and less than 5% maximum error in the Std of the displacement and velocity. Note that this error is due to both reduction in PC order and mesh resolution. Clearly non-matching discretization introduces larger error in the mean quantities compare to the standard deviation in contrast to the errors due to the PC order only (compare Figs. 5 and 7). Although the error is in the 1%–5% range, the results suggest that the localized mesh resolution, for this specific problem, affects the accuracy of the first mode of PC expansion more than the rest of the coefficients.

Next, to measure the convergence rate of the error at point P due to the mesh incompatibility, we define the following norm

$$\|\mathbf{e}_{\mathrm{MSTD}}(u_x)\| = \sqrt{\int_T \left[\overline{\mathrm{MSTD}}(u_x^*) - \mathrm{MSTD}(u_x) \right]^2 \mathrm{dt}}, \tag{33}$$

(a) Mean of displacement.

(b) Std of displacement.

(c) Mean of velocity.

(d) Std of velocity.

Fig. 5. The error in the mean and the standard deviation at point P due to uncertainty representation. The error is measured using Eq. (32) with $\overline{\text{MSTD}}$ being the solution using both MC ($\mathcal{E}_{MC}$) and PC6 ($\mathcal{E}_{PC}$), with compatible mesh $h = 0.03125$ m and uniform time step $\Delta t = 0.025$ s. The quantity MSTD is the solution using $PC4$ with compatible mesh $h = 0.03125$ m and uniform time step $\Delta t = 0.025$ s.
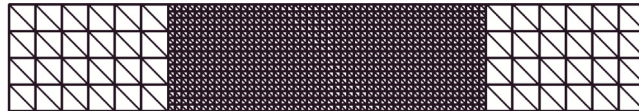
Fig. 6. Mesh (b) with mesh densities $h_1 = 0.125$ m, $h_2 = 0.03125$ m, and $h_3 = 0.125$ m.

where $\overline{\text{MSTD}}(u_x^*)$ represents either the mean or Std corresponding to the compatible mesh with $h = 0.03125$ m and $\text{MSTD}(u_x)$ is either the mean or Std using meshes (a)–(c). In all cases, fourth order PC expansion and uniform time increment $\Delta t_s = 0.025$ s are used. The convergence rates are shown in Fig. 8 for the mean and Std of the displacement and velocity at point P. Second order convergence rate with respect to the average mesh size is achieved for both the mean and Std (see [33] for deterministic convergence studies).

5.1.3. Effect of time asynchronicity

Next, we study the efficiency of the asynchronous time integration in reducing the computational cost of uncertainty quantification. In particular, we keep a fine time step in subdomain Ω_2 (subdomain containing the QOIs) and employ a coarser time discretization in subdomains Ω_1 and Ω_3. The asynchronous time ratios are listed in Table 2.

Fig. 9 shows the relative percentage error for the case of asynchronous time discretization (case (b) in Table 2) with matching meshes (mesh density $h = 0.03125$ m) and fourth order PC expansion. Once again, we use the error measures defined in Eq. (32). When coarsening the time step four times in the subdomains Ω_1 and Ω_3, less than 1% and 4% error in the mean and Std can be observed, respectively. These errors are due to both PC order reduction and asynchronous time discretization.

(a) Mean of displacement.

(b) Std of displacement.

(c) Mean of velocity.

(d) Std of velocity.
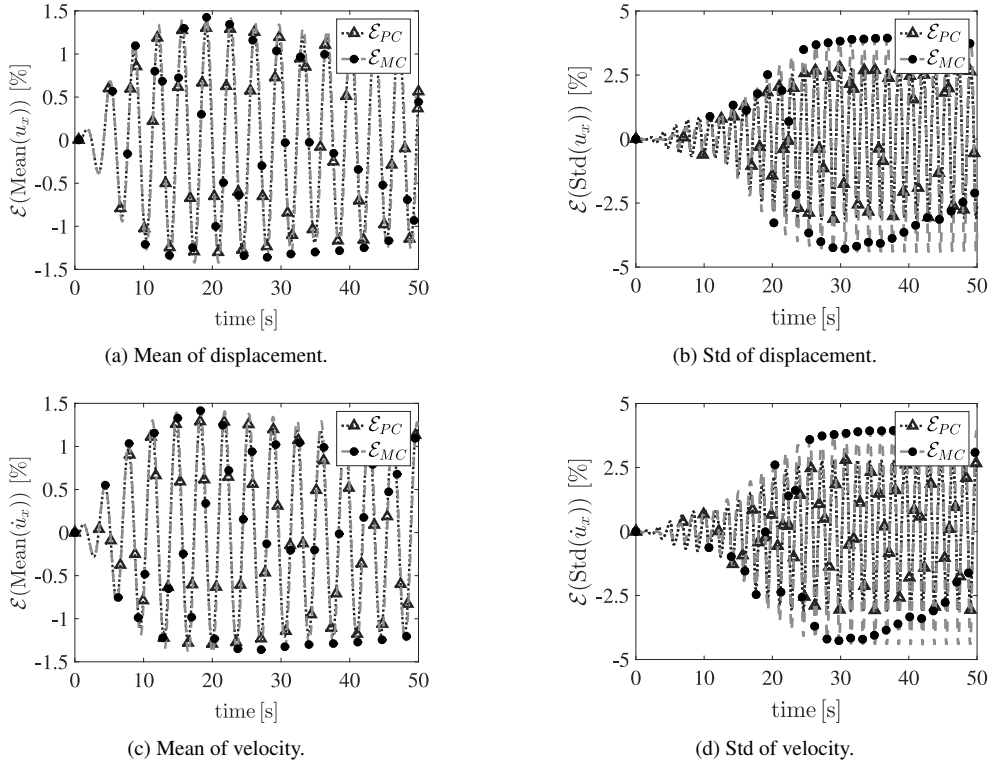
Fig. 7. The error in the mean and the standard deviation at point P due to mesh incompatibility. The error is measured using Eq. (32) with $\overline{\text{MSTD}}$ being the solution using both MC ($\mathcal{E}_{MC}$) and PC6 ($\mathcal{E}_{PC}$), with compatible mesh $h = 0.03125$ m and uniform time step $\Delta t = 0.025$ s. The quantity MSTD is the solution using $PC4$ with mesh incompatibility ratio of h_1:h_2:$h_3 = 1$:4:1 and uniform time step $\Delta t_s = 0.025$ s.

(a) Mean.

(b) Standard deviation.
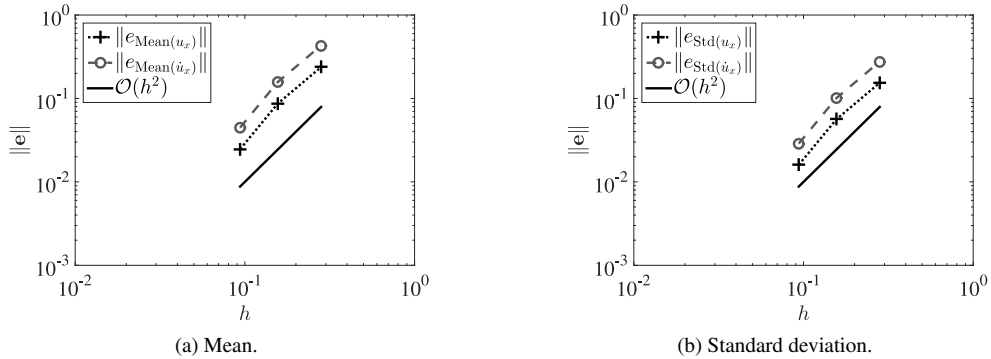
Fig. 8. Rate of convergence for (a) the mean and (b) the standard deviation at point P for the horizontal component of the displacement and velocity with respect to the average mesh size. Uniform $\Delta t_s = 0.025$ s and $PC4$ are used.

Next, we measure the rate of convergence of the error in the mean and Std at point P with respect to the synchronization time step. The same error norm defined in Eq. (33) is utilized. However, the reference quantity $\overline{\text{MSTD}}(u_x^*)$ is redefined as either the mean or Std corresponding to the synchronous time integration with $\Delta t = 0.025$ s and $\text{MSTD}(u_x)$ is either the mean or Std due to the asynchronous time discretization (see Table 2). In all cases, fourth order PC representation and matching meshes with $h = 0.03125$ m are used. The convergence rates are shown in Fig. 10 for the mean and Std of the displacement and velocity at point P. Second order convergence rate with respect to the synchronization time step is achieved (see [33] for deterministic convergence studies).

Table 2

Asynchronous time discretizations.

Scheme	Δt_1 [s]	Δt_2 [s]	Δt_3 [s]	$\Delta t_1{:}\Delta t_2{:}\Delta t_3$
(a)	0.05	0.025	0.05	1:2:1
(b)	0.10	0.025	0.10	1:4:1
(c)	0.20	0.025	0.20	1:8:1

(a) Mean of displacement.

(b) Std of displacement.

(c) Mean of velocity.

(d) Std of velocity.
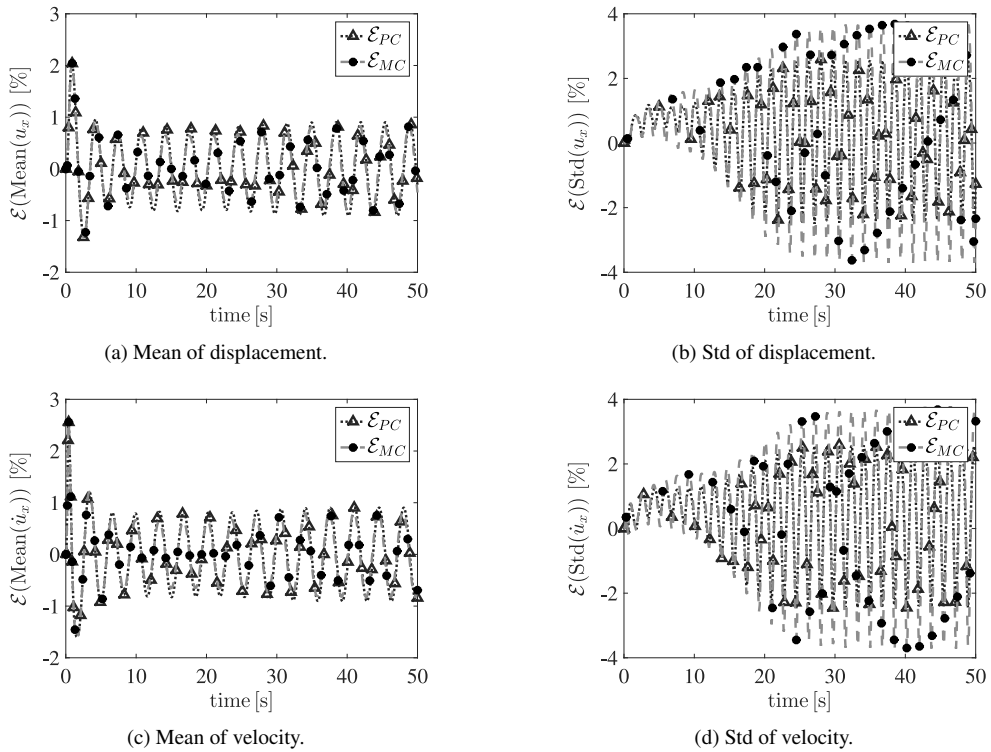
Fig. 9. The error in the mean and the standard deviation at point P due to asynchronous time integration. The error is measured using Eq. (32) with $\overline{\text{MSTD}}$ being the solution using both MC ($\mathcal{E}_{MC}$) and PC6 ($\mathcal{E}_{PC}$), with compatible mesh $h = 0.03125$ m and uniform time step $\Delta t = 0.025$ s. The quantity MSTD is the solution using $PC4$ with compatible mesh $h = 0.03125$ m and time synchronicity ratio of $\Delta t_1{:}\Delta t_2{:}\Delta t_3 = 1{:}4{:}1$.

(a) Mean.

(b) Standard deviation.
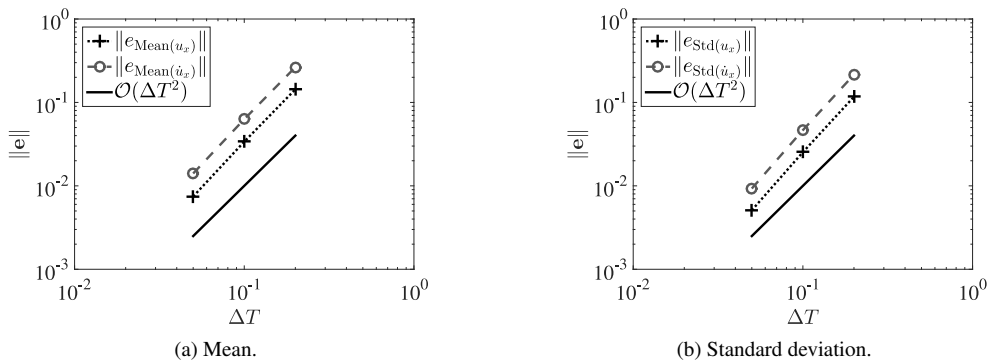
Fig. 10. Rate of convergence for (a) the mean and (b) the standard deviation at point P for the horizontal component of the displacement and velocity with respect to the synchronization time step ΔT. Matching meshes $h = 0.03125$ m and $PC4$ are used.

(a) Mean of displacement.

(b) Std of displacement.

(c) Mean of velocity.

(d) Std of velocity.
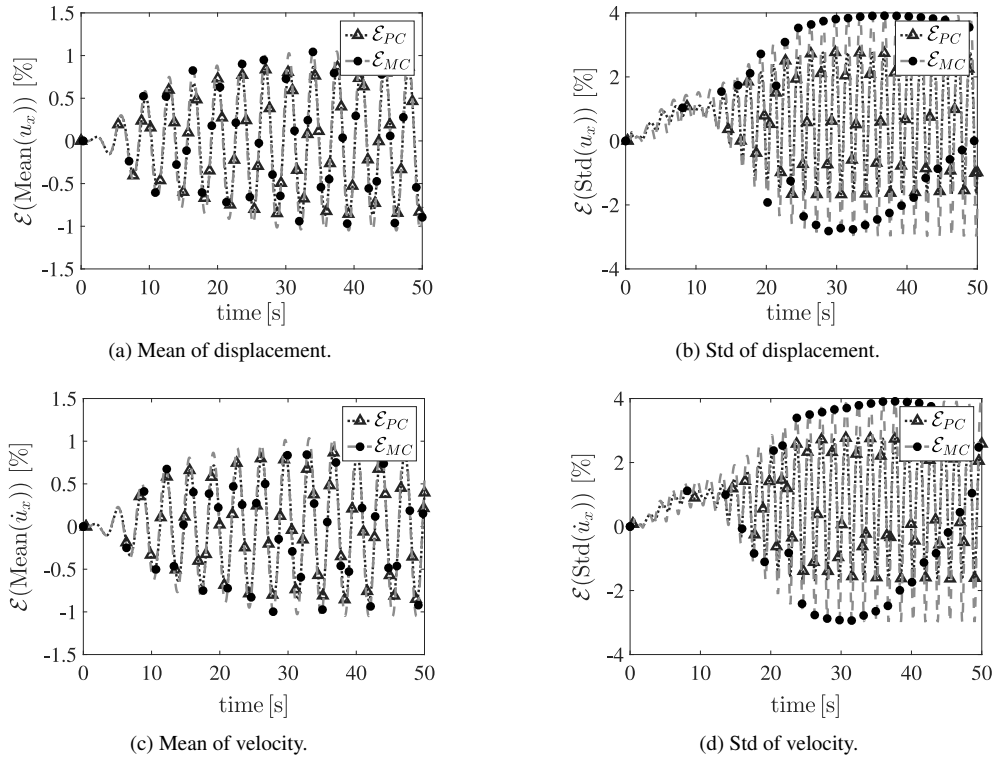
Fig. 11. The error in the mean and the standard deviation at point P due to the localized uncertainty. The error is measured using Eq. (32) with $\overline{\text{MSTD}}$ being the solution using both MC ($\mathcal{E}_{MC}$) and PC6 ($\mathcal{E}_{PC}$), with compatible mesh $h = 0.03125$ m and uniform time step $\Delta t = 0.025$ s. The quantity MSTD is the solution when the Young's modulus is a random field confined in Ω_2 while a reduced field is assumed in Ω_1 and Ω_3. $PC4$ is used with matching meshes $h = 0.03125$ m and uniform time step $\Delta t = 0.025$ s.

5.1.4. Effect of localized uncertainty

In conjunction with asynchronous space–time scheme, the computational cost of uncertainty quantification can be reduced further when the propagation media exhibits a confined stochastic nature. The effect of confining the variability of the material properties around the region of interest is investigated next. In general, this is a challenging task and often a problem dependent issue. The spatial confinement of uncertainty and the dimension of its representation should be carefully considered with the PC order of the response and the location of the QOIs. The correlation length of the random field can be used as an initial guide. We discuss some of these issues in the example provided in Section 5.2.

We assume that the Young's modulus is a random field and can be confined in Ω_2, while a reduced representation of uncertainty may be sufficient in subdomains Ω_1 and Ω_3:

$$E(\mathbf{x}, \boldsymbol{\xi}) = \begin{cases} E(\mathbf{x}, \boldsymbol{\xi}) & \mathbf{x} \in \Omega_2, \\ \tilde{E}(\mathbf{x}, \boldsymbol{\xi}) & \mathbf{x} \in \{\Omega_1, \Omega_3\}. \end{cases} \tag{34}$$

Here $\tilde{E}(\mathbf{x}, \boldsymbol{\xi})$ is a reduced random representation of the Young's modulus and $E(\mathbf{x}, \boldsymbol{\xi})$ is the full representation provided in Eq. (4).

First, we use one random variable to represent the random field in Ω_1 and Ω_3, while keeping two random variables in Ω_2. Fig. 11 shows the relative percentage error of the mean and Std of both the displacement and velocity at point P using Eq. (32). Matching meshes with mesh density $h = 0.03125$ m, synchronous time integration with $\Delta t = 0.025$ s, and fourth order PC are used. The errors in the displacement and velocity follow same trend. The maximum value of the error in the mean is about 1% and in the Std is about 4% for both the displacement and velocity.

Next, we use a deterministic model in both subdomains Ω_1 and Ω_3, and keep the stochastic model in subdomain Ω_2. In particular, only the mean value is used to represent the Young's modulus in subdomains Ω_1 and Ω_3. However,
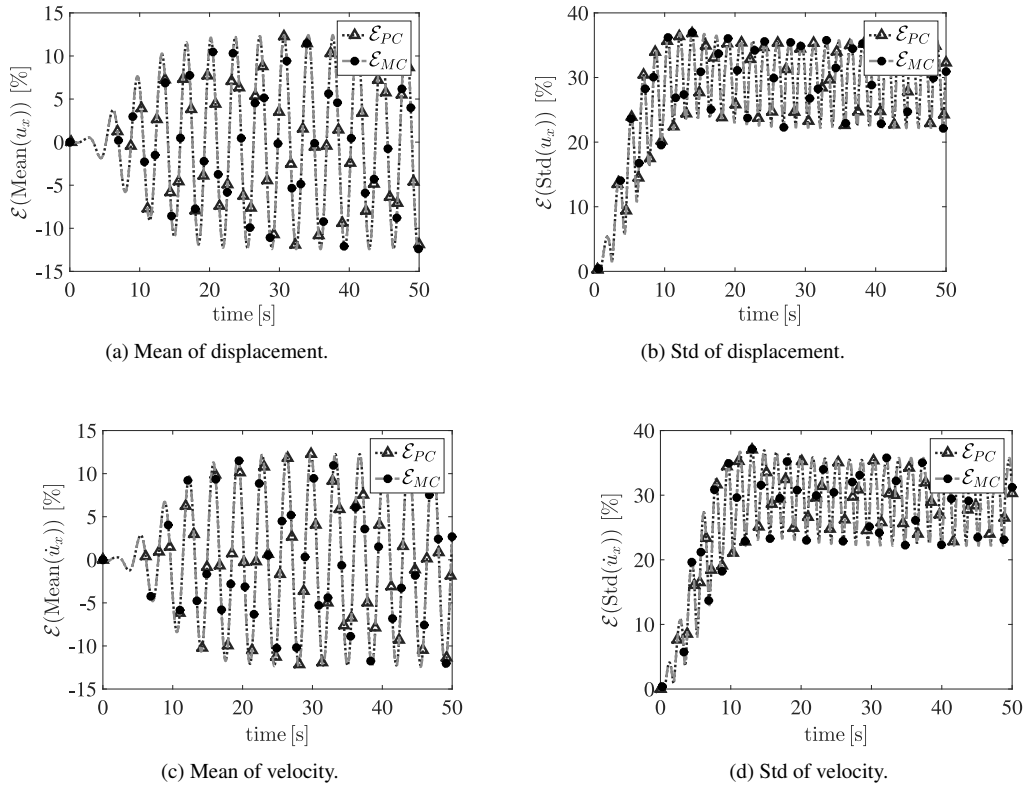
Fig. 12. The error in the mean and the standard deviation at point P due to the localized uncertainty. The error is measured using Eq. (32) with $\overline{\text{MSTD}}$ being the solution using both MC ($\mathcal{E}_{MC}$) and PC6 ($\mathcal{E}_{PC}$), with compatible mesh $h = 0.03125$ m and uniform time step $\Delta t = 0.025$ s. The quantity MSTD is the solution when the Young's modulus is a random field confined in Ω_2 while the mean field is assumed in Ω_1 and Ω_3. $PC4$ is used with matching meshes $h = 0.03125$ m and uniform time step $\Delta t = 0.025$ s.

two random variables are used in the subdomain Ω_2. For matching meshes with mesh density $h = 0.03125$ m, uniform time step $\Delta t = 0.025$ s, and fourth order PC expansion, Fig. 12 shows the relative error of the mean and standard deviation of both the displacement and velocity at point P using Eq. (32). The errors in the displacement and velocity follow the same trend. The errors in the mean and standard deviation are larger to those with $\tilde{E}(\mathbf{x}, \boldsymbol{\xi})$ represented by one random variable (compare Figs. 11 and 12). This is expected since in the second case the material properties across the subdomains are coupled through the mean value of the Young's modulus only.

Note that the error can be reduced by either enlarging the length of the uncertain subdomain Ω_2 or increasing the order of the coupling mechanism between the subdomains (i.e., higher representation of the random field can be considered in the region of interest, while a lower stochastic dimension can be assigned elsewhere). The latter approach is studied in Section 5.2 and the former approach is considered in what follows.

We define the confinement length for localized uncertainty as $l = (L - L_{\Omega_2})/L$, where $L = 3.0$ m is the size of the entire computational domain and $L_{\Omega_2} \in \{2.5, 2.0, 1.5, 1.0\}$ m represents the size of the uncertain subdomain Ω_2. In practice, the confinement length for localized uncertainty can be estimated using measurements as explained in the Appendix. The error norm defined in Eq. (33) is utilized. However, the reference quantity $\overline{\text{MSTD}}(u_x^*)$ is redefined as either the mean or Std corresponding to the case of unconfined uncertainty (i.e., the Young's modulus is a random field defined in the entire domain). Matching meshes with mesh density $h = 0.03125$ m, synchronous time step $\Delta t = 0.025$ s, and fourth order PC are used to study the convergence. The convergence rates are shown in Fig. 13 for the mean and Std of the displacement and velocity at point P. The first order convergence rate is achieved for both the displacement and velocity means at point P with respect to the confinement length of the localized uncertainty. A faster convergence rate can be observed for the Std of the displacement and velocity at point P.

(a) Mean.

(b) Standard deviation.
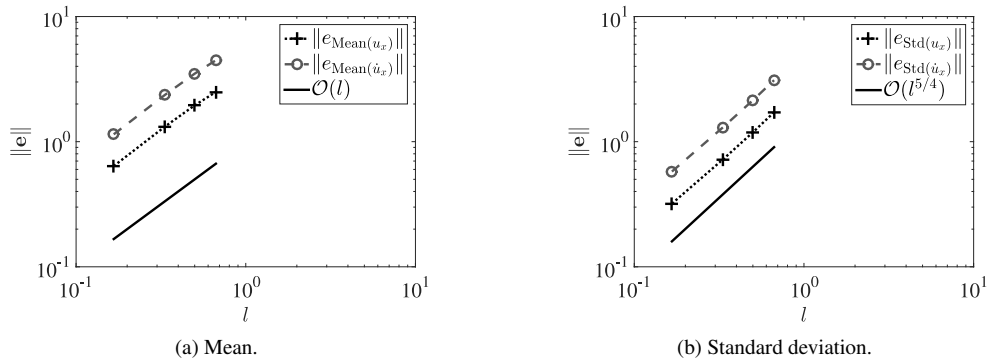
Fig. 13. Rate of convergence for (a) the mean and (b) the standard deviation at point P for the horizontal component of the displacement and velocity with respect to the confinement length $l = (L - L_{\Omega_2})/L$. Matching meshes $h = 0.03125$ m, uniform time step $\Delta t = 0.025$ s, and $PC4$ are used.

Table 3
Spatial discretization, temporal discretization, and random material representation.

	Ω_1	Ω_2	Ω_3
h [m]	0.12500	0.03125	0.12500
Δt [s]	0.100	0.025	0.100
E	E_0	$E(\mathbf{x}, \boldsymbol{\xi})$	E_0

5.1.5. Effects of mesh incompatibility, time asynchronicity and localized uncertainty

The total effect of mesh incompatibility, time asynchronicity, and localized uncertainty on reducing the computational cost of uncertainty quantification is investigated next. Specifically, a coarse mesh and large time steps are assigned to Ω_1 and Ω_3, where the mean field of the Young's modulus is used. In contrast, a finer mesh and small time steps are used in Ω_2, where the QOIs are located, in conjunction with the full random field. The properties are listed in Table 3 and we identify this simulation as *the reduced model*.

For the case of confined uncertainty with localized mesh and time resolutions in Fig. 14, we show the mean of the horizontal component of the displacement and velocity at point P. For the sake of comparison, on the same plot we show the results from matching meshes with mesh density $h = 0.03125$ m, uniform time step size $\Delta t = 0.025$ s, sixth order PC, and the Young's modulus being a random field in the entire domain. We label these results as *the full model*. The background light gray shaded area represents ± 2 Std of the full model, while the foreground dark gray shaded area represents ± 2 Std of the reduced model. Fig. 15 shows magnified insets of Fig. 14. In the scale of these magnified plots, there are only small differences between the mean results of both the full and reduced models. The confidence interval represented by ± 2 Std of the reduced model is smaller and lies within that of the full model. Note that the reduced model consists of 50% fewer elements, 1/4 the number of time steps, 13 fewer terms in PC representation, and no block coupling in the stiffness matrix of subdomains Ω_1 and Ω_3. Thus, large computational savings can be achieved using the reduced model.

5.2. Effect of the stochastic coupling mechanism

The accuracy of the proposed algorithm for localized UQ can be enhanced by increasing the dimension of the coupling mechanism between the subdomains, yet retaining the data reduction. A higher dimensional random field representation (i.e., Mth) can be considered in the region of interest, while a lower dimensional representation (i.e., 0th, 1st, 2nd, ..., $(M - 1)$th) can be assigned elsewhere. In the following example, we study the error introduced by the finite dimensional representation of the coupling mechanism. In particular, we consider an elastic wave propagation in a solid *dog–bone* like specimen as shown in Fig. 16. The computational domain is decomposed into three subdomains with material and discretization parameters shown in the Fig. 16. We take Young's modulus to be
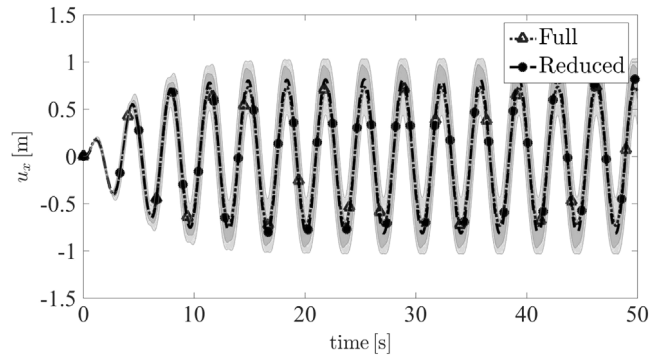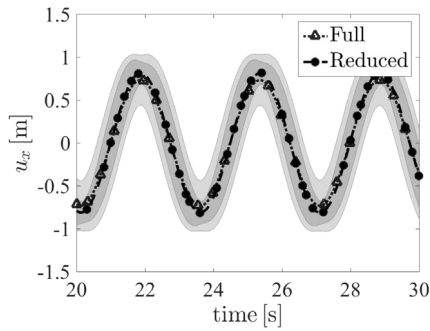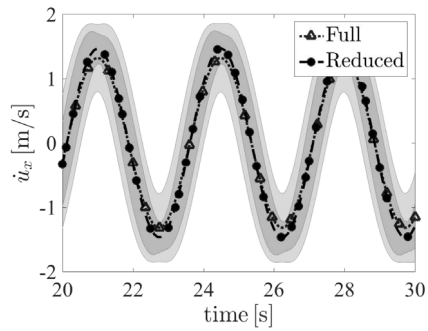
(a) Displacement.
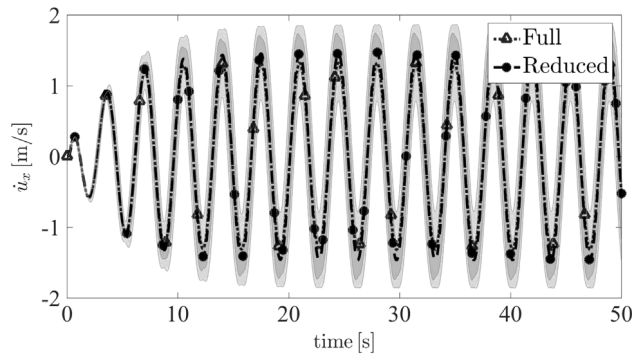
(b) Velocity.

Fig. 14. The mean and ±2 Std of the horizontal component of (a) displacement and (b) velocity at point P. The background light gray shaded area represents ±2 Std of the full model, while the foreground dark gray shaded area represents ±2 Std of the reduced model.
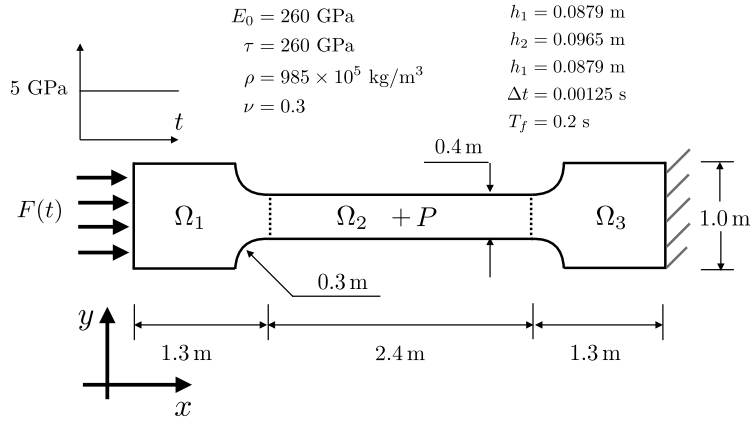

(a) Displacement.

(b) Velocity.

**Fig. 15.** Magnified insets of the results shown in Fig. 14. The background light gray shaded area represents ±2 Std of the full model, while the foreground dark gray shaded area represents ±2 Std of the reduced model.

a random field with the exponential covariance function given by Eq. (31) and correlation lengths $b_x = 5.0\,\text{m}$ and $b_y = 2.0\,\text{m}$, respectively.

In Fig. 17, we show the mean and Std of the displacement and velocity at point $P(2.5, 0.5)\,\text{m}$. The results are presented with respect to the dimension of the coupling mechanism (defined as the number of common random variables in the KLE that are shared among the subdomains). We use six dimensional random field, $M = 6$, to represent the Young's modules in subdomain Ω_2, while we reduce the representation in subdomains Ω_1 and Ω_3 to

Fig. 16. A dog–bone like specimen impacted at the left end while the right end is fixed. The QOIs are the displacement and velocity at point $P(2.5, 0.5)$ m.
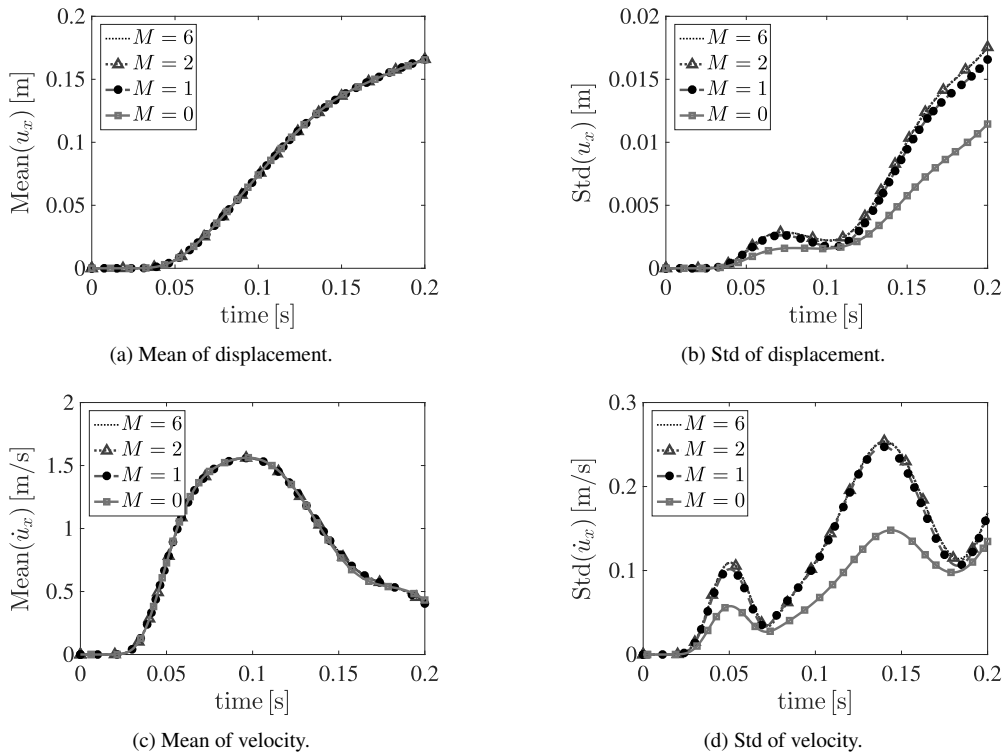
Fig. 17. The mean and Std of the displacement and velocity at point P. Here M indicates the number of random variables in KLE that are common across subdomains (i.e., the random variables used to represent uncertainty in subdomains Ω_1 and Ω_3). Note that for all cases six dimensional random field $M = 6$ is used in subdomain Ω_2.

$M = 2$, $M = 1$, and $M = 0$, respectively. The results suggest that the reduce representation even with $M = 0$ can capture the mean response reasonably well. However for the Std, the zero order representation $M = 0$ is able to capture the overall behavior with less accuracy.

Fig. 18 shows the relative percentage error of the Std of the displacement and velocity at point P with respect to the dimension of the coupling mechanism. When using a deterministic model in Ω_1 and Ω_3 ($M = 0$), the maximum percentage errors in the Std of the displacement and velocity are about 35% and 40%, respectively. However when

(a) Std of displacement.

(b) Std of velocity.
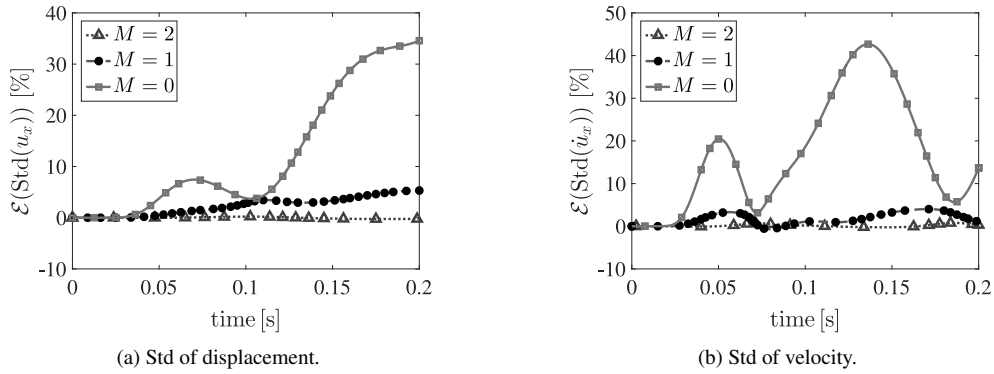
Fig. 18. The error in the Std of the displacement at point P with respect to the dimension of the coupling mechanism (i.e., the number of common random variables in KLE). The error is measured using Eq. (32) with $\overline{\text{MSTD}}$ being the Std corresponding to the case when using $M = 6$ for all of the subdomains.

using $M = 2$ in Ω_1 and Ω_3, the maximum percentage errors are reduced to about 0.2% and 0.8% for the displacement and velocity, respectively. Thus, enriching the coupling mechanism by adding more random variables to be propagated across the interfaces leads to an error reduction in the Std.

Next, we show in (Fig. 19) the block sparsity structure of the global dual–primal system, Eqs. (25)–(30), with respect to the dimension of the coupling mechanism. The block sparsity is due to the orthogonal properties of the PC representation of the random field. Fig. 19(a) displays the full representation of random field using $M = 6$ in the three subdomains, while (Fig. 19(d)) shows the maximum reduction in representation when using a deterministic model for Ω_1 and Ω_3 (e.g., see circle highlight in (Figs. 19(a) and (d)) for Ω_1). As the dimension of the coupling mechanism increases, off-diagonal blocks are populated at the subdomain level. Note that for $M = 0$ (Fig. 19(d)), the stiffness matrices for Ω_1 and Ω_3 are block diagonal. Furthermore for $M = 2$, a reduction of 25% in the fill-in of the full system is obtained (see (Figs. 19(a) and (b))). This leads to faster Schur complement construction, and thus faster and easier solution time.

As alluded to previously, the identification of the UQ localization region is problem dependent. The region of interest can be specified based on the localization features of the solution, user define/interest, the correlation length of the random field and measurement data. For problems where a region of interest is not evident, the Bayesian inference can be utilized as explained in the Appendix.

Fig. 20 shows the effect of the localization region (assigning random properties to different subdomains) on the QOIs. In particular, Fig. (20a) presents the log of the probability density function (pdf) of the displacement at point P at the final time of the simulation $T_f = 0.2$ s. We consider three localization regions to represent the reduced model: (a) Ω_1 is random ($M = 2$) while Ω_2 and Ω_3 are deterministic ($M = 0$), (b) Ω_3 is random ($M = 2$) while Ω_1 and Ω_2 are deterministic ($M = 0$), (c) Ω_2 is random ($M = 2$) while Ω_1 and Ω_3 are deterministic ($M = 0$). The results are compared with the full model where all three subdomains are assigned random properties with ($M = 6$). The results suggest that the reduced model (c) (assigning random properties to the region around the QOIs) gives the most accurate results. To quantify the error in the pdf's, we show in Fig. (20b) the Kullback–Leibler divergence of the reduced models pdf's to that of the full model. The Kullback–Leibler divergence is defined as

$$D_{KLd}(\pi_r \parallel \pi_f) = \int \pi_r(z) \log \left(\frac{\pi_r(z)}{\pi_f(z)} \right) dz, \tag{35}$$

where π_r and π_f are the pdf's of the reduced and full models, respectively. Clearly, the density of reduced model (c) is closest to the pdf of the full model.

5.3. Impact problem

For a more realistic engineering application of PASTA-DDM-UQ, we consider a sandwich plate impacted by a projectile [33,43]. The material properties in both the core and skin plates can be uncertain. However, it was shown
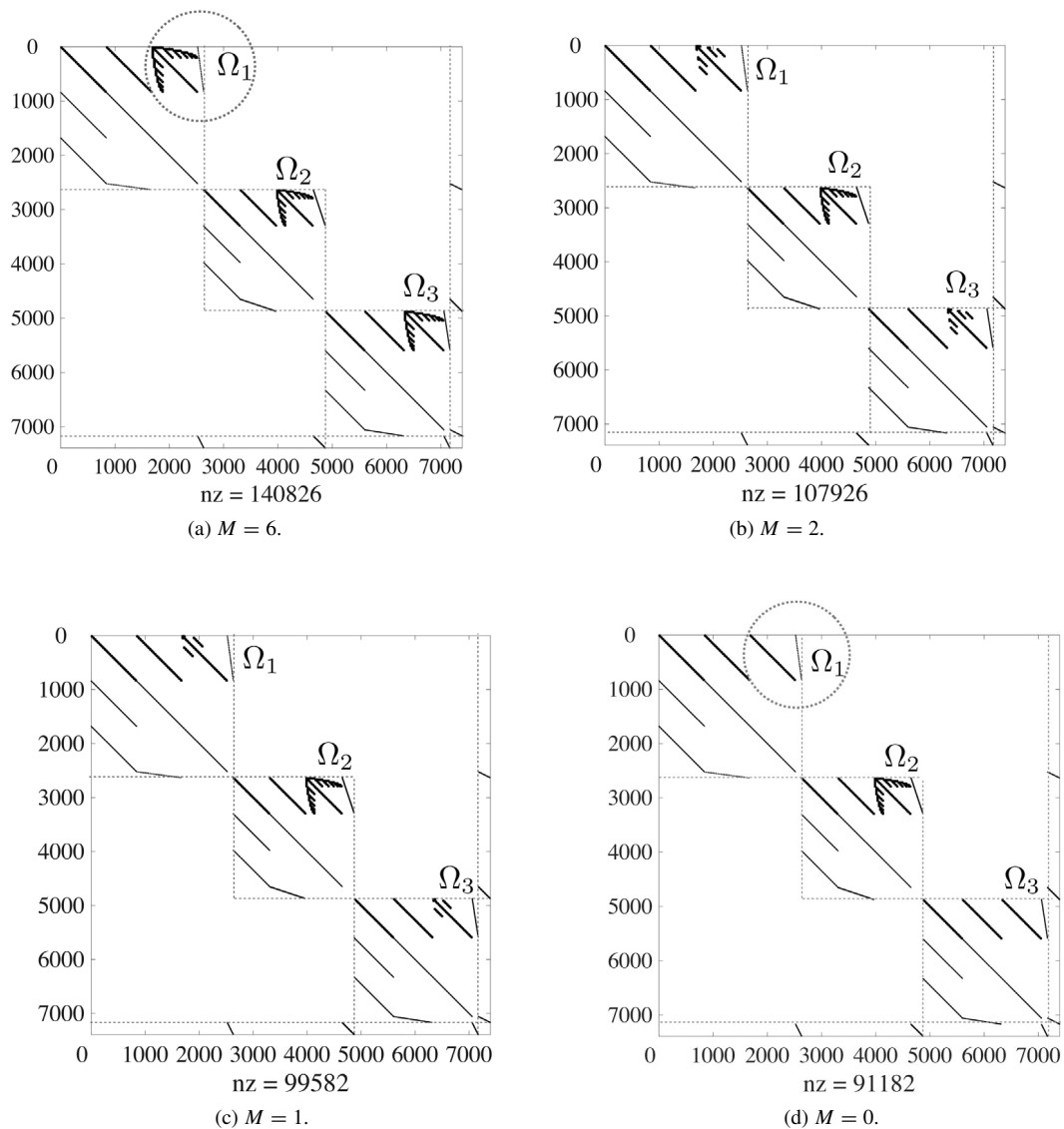
Fig. 19. The sparsity structure of the global dual–primal system, Eqs. (25)–(30), with respect to the dimension of the coupling mechanism (i.e., the number of common random variables in KLE). The variable nz represents the number of nonzero elements in the matrix. For the deterministic sparsity structure, please see Fig. 4 in [33].

in [33] that there are two scales of dynamics in this impact problem. A fast dynamics under the impact zone and a slow wave propagation in the regions away from the projectile impact. This localization feature of the response suggests that the cost of uncertainty quantification can be reduced by localizing the mesh and time resolutions and confining the uncertain variability of the material properties within the impact region only.

The following properties are considered for the numerical implementation. The thin skin plates have mean material properties $E = 70$ GPa, $\nu = 0.3$, $\rho = 2700$ kg/m^3 and the thick soft core has $E = 7.78$ GPa, $\nu = 0.3$, $\rho = 900$ kg/m^3. The physical dimensions are as follows: $b_1 = 2$ mm, $b_2 = 16$ mm, $l_1 = 80$ mm, and $l_2 = 40$ mm. The projectile is modeled as a traction with a ramp function that reaches its peak value 100 kN/m in 1×10^{-5} s. The final time for the simulation is $T_f = 2 \times 10^{-5}$ s. The subdomain material properties, spatial, and temporal discretization parameters are given in Table 4.

(a) Probability density function (pdf).

(b) Kullback–Leibler divergence.
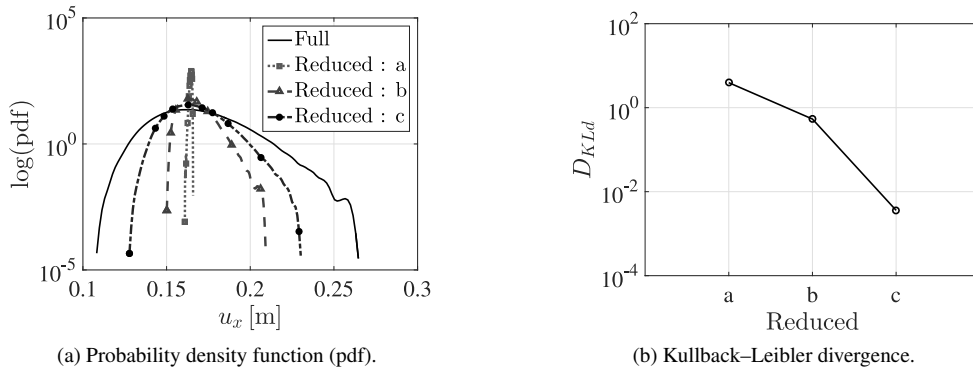
Fig. 20. Effect of the localization region: (a) the probability density functions of the displacement at P using the full and reduced models, (b) Kullback–Leibler distance.
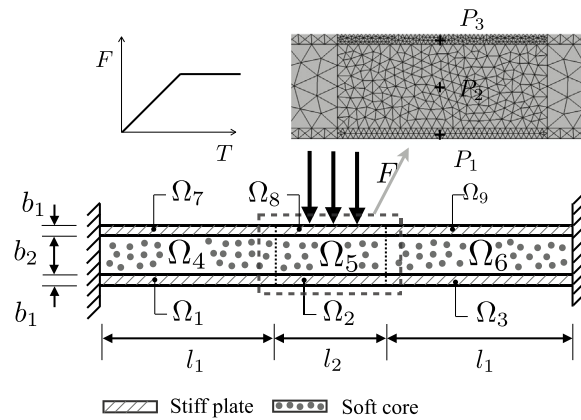
Fig. 21. A schematic diagram of a composite sandwich plate impacted by a projectile. The QOIs are the displacement and velocity at points $P_1(100, 1)$ mm, $P_2(100, 10)$ mm, and $P_3(100, 19)$ mm. The physical dimensions are $b_1 = 2$ mm, $b_2 = 16$ mm, $l_1 = 80$ mm, and $l_2 = 40$ mm [33].

Table 4
The mean material properties, spatial, and temporal discretizations of the composite plate.

Subdomain	E_s [GPa]	ρ_s [kg/m^3]	No. nodes	No. elem	Δt_s [s]
Ω_1	70	2700	78	87	1×10^{-7}
Ω_2	70	2700	126	166	5×10^{-8}
Ω_3	70	2700	78	87	1×10^{-7}
Ω_4	7.78	900	90	136	2×10^{-7}
Ω_5	7.78	900	239	420	2×10^{-7}
Ω_6	7.78	900	90	136	2×10^{-7}
Ω_7	70	2700	78	87	1×10^{-7}
Ω_8	70	2700	225	341	4×10^{-8}
Ω_9	70	2700	78	87	1×10^{-7}

For this uncertainty quantification study, we consider the Young's modulus to be a random field defined by KLE. The correlation lengths used for the exponential covariance function, Eq. (31), are $b_x = 400$ mm and $b_y = 40$ mm. The coefficient of variation is CoV $= \tau/E_0 = 15\%$. Two random variables and the fourth order PC are used.

The QOIs are the displacement and velocity at points P_1, P_2, and P_3 along the center line $x = 100$ mm (see marks in Fig. 21). We consider the following cases: (i) uncertainty is confined in the skin plates Ω_1, Ω_2, Ω_3, Ω_7, Ω_8, Ω_9, (ii) uncertainty is confined in the core Ω_4, Ω_5, Ω_6, (iii) uncertainty is confined within the subdomains under the impact zone Ω_2, Ω_5, Ω_8. The mean displacement and velocity of these three cases with ± 2 Std error bars are shown in Fig. 22.
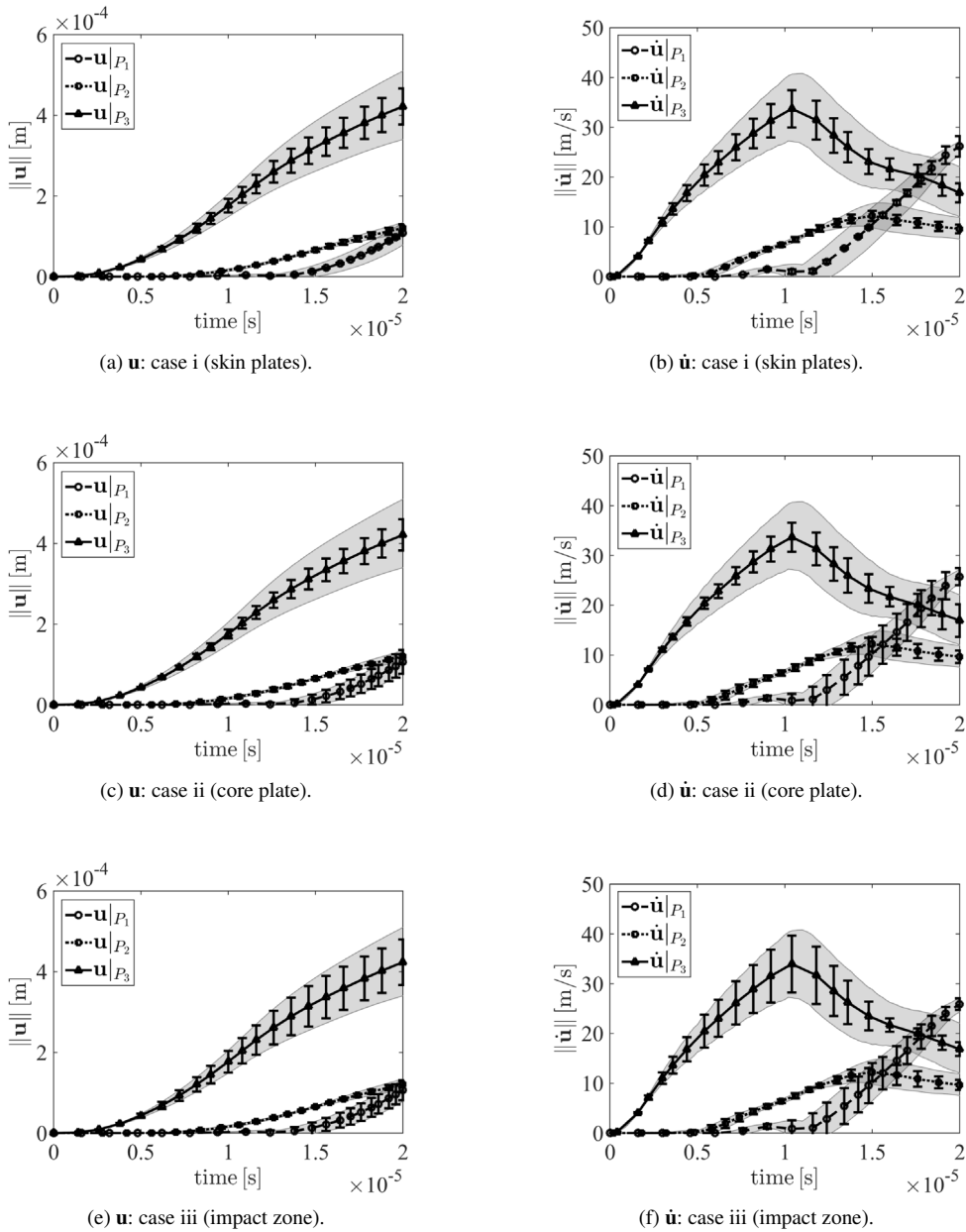
Fig. 22. The mean and ± 2 Std error bars of the displacement and velocity at points along the center line. The top panel (a & b) uncertainty is confined in the skin plates (case i). The middle panel (c & d) uncertainty is confined in the core (case ii). The bottom panel (e & f) uncertainty is confined within the impact zone (case iii). The shaded area represents ± 2 Std of the full model.

The background gray shaded area represents ± 2 Std of the full model when uncertainty is considered in the entire domain using fourth order PC. Since the solution has a localized feature manifested in the fast dynamics under the impact zone, confining the variability of the material properties within the impact zone gives the accurate results with the smallest computing efforts for case (iii). Figs. 22(e) and (f) indicate that the uncertainty in the material parameters under the impact zone results in the largest error bars for the output displacements and velocities. Moreover, these error bars approach the background shaded area which represents ± 2 Std of the full model.
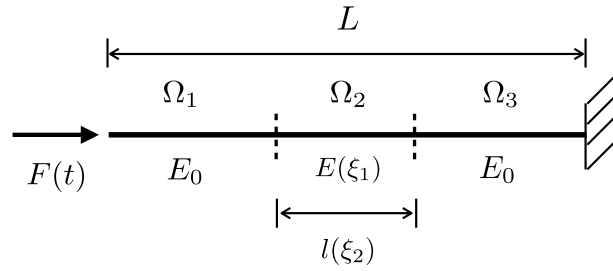
Fig. A.23. One-dimensional bar subjected to an impact loading.

6. Conclusions

We have developed an asynchronous space and time computational algorithm with localized uncertainty quantification. The framework is based on the recently proposed PASTA-DDM algorithm in conjunction with the intrusive polynomial chaos expansion for the stochastic representation that can be efficiently localized to selected subdomains. The proposed algorithm is customized to reduce the computational cost of uncertainty quantification in problems featuring localized phenomenon and described by stochastic PDE's (i.e., PDE's with random coefficients). In the region of interest, a rich stochastic model with high mesh and time resolutions is used, while a low dimensional stochastic representation with coarse spatial and temporal resolutions are allowed apart from the region of interest. We verify our algorithm with the traditional Monte-Carlo sampling technique and study different scenarios to reduce the computational cost of uncertainty quantification. For the elastic wave propagation problem, the algorithm shows second order convergence rate in the mean and standard deviation of both the displacement and velocity with respect to mesh size and time increment. Furthermore, the first order convergence rate is achieved with respect to the localization length. The application of PASTA-DDM-UQ to an impact problem shows that localizing the random variability of the material parameters under the impact zone gives the closest results to the case when uncertainty is considered in the entire domain.

Appendix. Data driven decomposition

In this appendix, we highlight a strategy of a model decomposition to localize uncertainty in a region of interest (see Section 5.1.4). In PASTA-DDM-UQ, there are two levels of domain partitioning: (i) a *coarse grain level* is the decomposition according to the material interfaces and the localized features, (ii) a *fine grain level* is the domain decomposition driven by the parallelism and the computer hardware requirements (i.e., memory and processors speed). To obtain the coarse grain level decomposition, we rely on experimental measurements to estimate the optimal partitioning of the physical domain. To this end, Bayesian inference technique is utilized. In Bayesian inference, the prior knowledge is updated to posterior using noisy data and uncertain model [6,44]. The update is based on Bayes' rule which defines the posterior probability density function as

$$p(\chi|d) = \frac{p(\chi)p(d|\chi)}{p(d)} = \frac{p(\chi)p(d|\chi)}{\int p(\chi)p(d|\chi)\mathrm{d}\chi}, \tag{A.1}$$

where χ is the uncertain parameter to be estimated, d is the measurement of an observable quantity, $p(\chi|d)$ is the posterior probability density function, $p(\chi)$ is the prior probability density function, and $p(d|\chi)$ denotes the likelihood.

To illustrate this idea, we consider a one-dimensional bar subjected to an impact loading as shown in Fig. A.23. The bar is decomposed into three subdomains and the task is to estimate the length of Ω_2 from noisy (experimental) data. Deterministic material properties are assigned to subdomains Ω_1 and Ω_3, while in Ω_2 the Young's modulus is defined as a random variable. We assume the differences between the model and the experimental data be independent
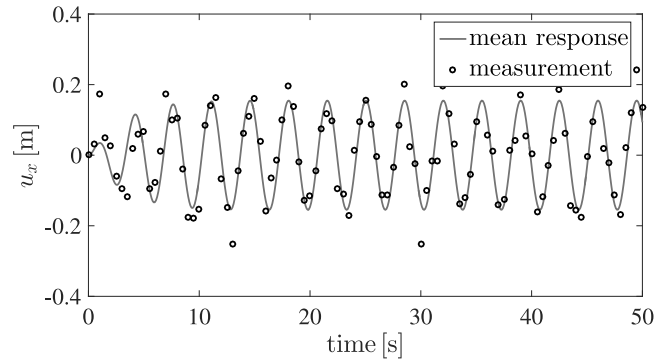
Fig. A.24. The displacement in the middle of the bar using the mean properties and the noisy measurements.

(a) Probability density function.
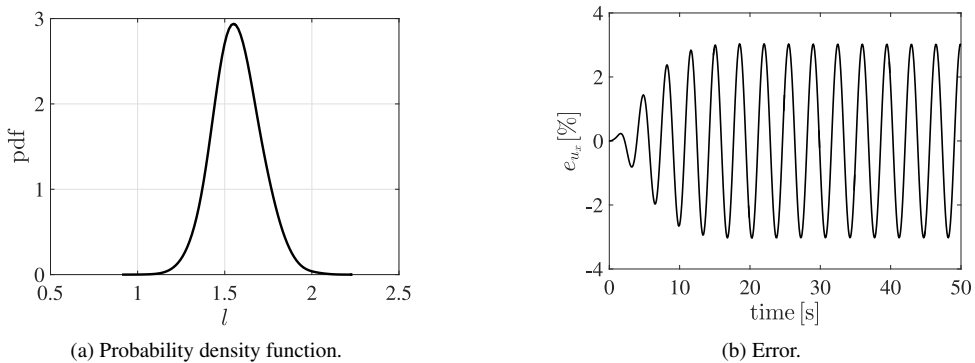
(b) Error.

Fig. A.25. The posterior probability density function and the error due to the estimated parameters.

and identically distributed Gaussian random variables. This results a likelihood function for the unknown parameters as the product of normal probability density functions. We define a PC surrogate model [45] for the displacement at a point in the middle of the domain (at $L/2$). The Young's modulus and the decomposition length for the subdomain Ω_2 are defined as:

$$E(\xi_1) = E_0(1 + 0.15\,\xi_1), \tag{A.2}$$

$$l(\xi_2) = l_0(1 + 0.5\,\xi_2). \tag{A.3}$$

Here, $E_0 = 81.9\,\text{kPa}$, $l_0 = 1.5$ m, and $\xi_i \sim \mathcal{U}(-1, 1)$. The synthetic data is generated based on the mean properties (E_0, l_0) and 5% Gaussian noise to mimic the experimental evidence. In practice, this data can come from experiments. Fig. A.24 shows the response using the mean properties and the sparse noisy data. The two-dimensional fourth order Legendre polynomial is used for the surrogate model. Markov Chain Monte Carlo (MCMC) sampling technique [46] is used to estimate the posterior density for the decomposition length as shown in (Fig. A.25a). Note that the estimated mean of the decomposition length is 1.569 m and the standard deviation is 0.131 m. (Fig. A.25b) shows the relative error between the mean response and the response using the estimated mean properties of the parameters. The error is defined as

$$e_{u_x} = \frac{u_x^{mean} - u_x^{estm}}{\max(u_x^{mean})} \times 100\,[\%], \tag{A.4}$$

where u_x^{mean} is the solution using the mean properties and u_x^{estm} is the solution using the estimated parameters.

References

[1] Karel Matouš, Marc G.D. Geers, Varvara G. Kouznetsova, Andrew Gillman, A review of predictive nonlinear theories for multiscale modeling of heterogeneous materials, J. Comput. Phys. 330 (2017) 192–220.

[2] Matthew Mosby, Karel Matouš, Computational homogenization at extreme scales, Extreme Mech. Lett. 6 (2016) 68–74.

[3] Roger G. Ghanem, Uncertainty quantification in computational and prediction science, Internat. J. Numer. Methods Engrg. 80 (6–7) (2009) 671–672.

[4] Aleksandr Chernatynskiy, Simon R. Phillpot, Richard LeSar, Uncertainty quantification in multiscale simulation of materials: A prospective, Annu. Rev. Mater. Res. 43 (2013) 157–182.

[5] Olivier Le Maître, Omar M. Knio, Spectral Methods for Uncertainty Quantification: With Applications to Computational Fluid Dynamics, Springer Science & Business Media, 2010.

[6] Ralph C. Smith, Uncertainty Quantification: Theory, Implementation, and Applications, Vol. 12, SIAM, 2013.

[7] Roger G. Ghanem, Pol D. Spanos, Stochastic Finite Elements: A Spectral Approach, Courier Corporation, 2003.

[8] Dongbin Xiu, Numerical Methods for Stochastic Computations: A Spectral Method Approach, Princeton University Press, 2010.

[9] Yalchin Efendiev, Thomas Hou, Wuan Luo, Preconditioning Markov chain Monte Carlo simulations using coarse-scale models, SIAM J. Sci. Comput. 28 (2) (2006) 776–803.

[10] Habib N. Najm, Uncertainty quantification and polynomial chaos techniques in computational fluid dynamics, Annu. Rev. Fluid Mech. 41 (2009) 35–52.

[11] Howard C. Elman, Christopher W. Miller, Eric T. Phipps, Raymond S. Tuminaro, Assessment of collocation and Galerkin approaches to linear diffusion equations with random data, Int. J. Uncertain. Quantif. 1 (1) (2011).

[12] Roger G. Ghanem, Robert M. Kruger, Numerical solution of spectral stochastic finite element systems, Comput. Methods Appl. Mech. Engrg. 129 (3) (1996) 289–303.

[13] Anthony Nouy, Recent developments in spectral stochastic methods for the numerical solution of stochastic partial differential equations, Arch. Comput. Methods Eng. 16 (3) (2009) 251–285.

[14] O.P. Le Maıtre, O.M. Knio, B.J. Debusschere, H.N. Najm, R.G. Ghanem, A multigrid solver for two-dimensional stochastic diffusion equations, Comput. Methods Appl. Mech. Engrg. 192 (41) (2003) 4723–4744.

[15] Eveline Rosseel, Tim Boonen, Stefan Vandewalle, Algebraic multigrid for stationary and time-dependent partial differential equations with stochastic coefficients, Numer. Linear Algebra Appl. 15 (2–3) (2008) 141–163.

[16] Catherine E. Powell, Howard C. Elman, Block-diagonal preconditioning for spectral stochastic finite-element systems, IMA J. Numer. Anal. 29 (2) (2009) 350–375.

[17] Bedřich Sousedík, Roger G. Ghanem, Eric T. Phipps, Hierarchical Schur complement preconditioner for the stochastic Galerkin finite element methods, Numer. Linear Algebra Appl. 21 (1) (2014) 136–151.

[18] Debraj Ghosh, Philip Avery, Charbel Farhat, A FETI-preconditioned conjugate gradient method for large-scale stochastic finite element problems, Internat. J. Numer. Methods Engrg. 80 (6–7) (2009) 914–931.

[19] Ivana Pultarová, Hierarchical preconditioning for the stochastic Galerkin method: upper bounds to the strengthened CBS constants, Comput. Math. Appl. 71 (4) (2016) 949–964.

[20] Waad Subber, Abhijit Sarkar, Dual-primal domain decomposition method for uncertainty quantification, Comput. Methods Appl. Mech. Engrg. 266 (2013) 112–124.

[21] Waad Subber, Abhijit Sarkar, A domain decomposition method of stochastic PDEs: An iterative solution techniques using a two-level scalable preconditioner, J. Comput. Phys. 257 (2014) 298–317.

[22] Waad Subber, Sébastien Loisel, Schwarz preconditioners for stochastic elliptic PDEs, Comput. Methods Appl. Mech. Engrg. 272 (2014) 34–57.

[23] Abhijit Sarkar, Nabil Benabbou, Roger Ghanem, Domain decomposition of stochastic PDEs: theoretical formulations, Internat. J. Numer. Methods Engrg. 77 (5) (2009) 689–701.

[24] George Stavroulakis, Dimitris G. Giovanis, Manolis Papadrakakis, Vissarion Papadopoulos, A new perspective on the solution of uncertainty quantification and reliability analysis of large-scale problems, Comput. Methods Appl. Mech. Engrg. 276 (2014) 627–658.

[25] Prasanth B. Nair, Andrew J. Keane, Stochastic reduced basis methods, AIAA J. 40 (8) (2002) 1653–1664.

[26] Sondipon Adhikari, A reduced spectral function approach for the stochastic finite element analysis, Comput. Methods Appl. Mech. Engrg. 200 (21) (2011) 1804–1821.

[27] Alireza Doostan, Roger G. Ghanem, John Red-Horse, Stochastic model reduction for chaos representations, Comput. Methods Appl. Mech. Engrg. 196 (37) (2007) 3951–3966.

[28] Srikara Pranesh, Debraj Ghosh, Addressing the curse of dimensionality in SSFEM using the dependence of eigenvalues in KL expansion on domain size, Comput. Methods Appl. Mech. Engrg. 311 (2016) 457–475.

[29] C. Larrabee Winter, Daniel M. Tartakovsky, Mean flow in composite porous media, Geophys. Res. Lett. 27 (12) (2000) 1759–1762.

[30] C. Larrabee Winter, Daniel M. Tartakovsky, Groundwater flow in heterogeneous composite aquifers, Water Resour. Res. 38 (8) (2002).

[31] Régis Cottereau, Didier Clouteau, H. Ben Dhia, Cédric Zaccardi, A stochastic-deterministic coupling method for continuum mechanics, Comput. Methods Appl. Mech. Engrg. 200 (47) (2011) 3280–3288.

[32] Mohammad Hadigol, Alireza Doostan, Hermann G. Matthies, Rainer Niekamp, Partitioned treatment of uncertainty in coupled domain problems: A separated representation approach, Comput. Methods Appl. Mech. Engrg. 274 (2014) 103–124.

[33] Waad Subber, Karel Matouš, Asynchronous space–time algorithm based on a domain decomposition method for structural dynamics problems on non-matching meshes, Comput. Mech. 57 (2) (2016) 211–235.

[34] Phillip L. Gould, Introduction to Linear Elasticity, Springer, 2013.

[35] Bert J. Debusschere, Habib N. Najm, Philippe P. Pébay, Omar M. Knio, Roger G. Ghanem, Olivier P. Le Maître, Numerical challenges in the use of polynomial chaos representations for stochastic processes, SIAM J. Sci. Comput. 26 (2) (2004) 698–719.

[36] Roger Ghanem, George Saad, Alireza Doostan, Efficient solution of stochastic systems: application to the embankment dam problem, Struct. Saf. 29 (3) (2007) 238–251.

[37] Paolo L. Gatti, Applied Structural and Mechanical Vibrations: Theory and Methods, CRC Press, 2014.
[38] Ivo Babuška, Raúl Tempone, Georgios E. Zouraris, Solving elliptic boundary value problems with uncertain coefficients by the finite element method: the stochastic formulation, Comput. Methods Appl. Mech. Engrg. 194 (12) (2005) 1251–1294.
[39] D. Xiu, Fast numerical methods for stochastic computations: A review, Commun. Comput. Phys. 5 (2009) 242–272.
[40] Frédéric Magoulès, François-Xavier Roux, Lagrangian formulation of domain decomposition methods: A unified theory, Appl. Math. Model. 30 (7) (2006) 593–615.
[41] Didier Lucor, Chau-Hsing Su, George Em Karniadakis, Generalized polynomial chaos and random oscillators, Internat. J. Numer. Methods Engrg. 60 (3) (2004) 571–596.
[42] Abhishek Kundu, Sondipon Adhikari, Transient response of structural dynamic systems with parametric uncertainty, J. Eng. Mech. 140 (2) (2013) 315–331.
[43] Arun Prakash, Ertugrul Taciroglu, Keith D. Hjelmstad, Computationally efficient multi-time-step method for partitioned time integration of highly nonlinear structural dynamics, Comput. Struct. 133 (2014) 51–63.
[44] Andrew Gelman, John B. Carlin, Hal S. Stern, Donald B. Rubin, Bayesian Data Analysis, Vol. 2, Chapman & Hall/CRC Boca Raton, FL, USA, 2014.
[45] Youssef M. Marzouk, Habib N. Najm, Larry A. Rahn, Stochastic spectral methods for efficient bayesian solution of inverse problems, J. Comput. Phys. 224 (2) (2007) 560–586.
[46] Heikki Haario, Marko Laine, Antonietta Mira, Eero Saksman, DRAM: Efficient adaptive MCMC, Stat. Comput. 16 (4) (2006) 339–354.